https://doi.org/10.5194/se-2020-47
Preprint. Discussion started: 4 May 2020

Solid Earth Discussions

Benchmark study using a multi-scale, multi-methodological approach for the petrophysical characterization of reservoir sandstones

Peleg Haruzi[1,2], Regina Katsman[1], Matthias Halisch[3], Nicolas Waldmann[1], and Baruch Spiro[1,4]

[1] The Dr. Moses Strauss Department of Marine Geosciences, Faculty of Natural Sciences, The University of Haifa, Haifa, Mount Carmel 3498838, Israel

[2] Agrosphere Institute, IBG-3, Institute of Bio- and Geosciences, Forschungszentrum Jülich GmbH, Germany

[3] Leibniz Institute for Applied Geophysics, Dept. 5 – Petrophysics & Borehole Geophysics, Stilleweg 2, D-30655 Hannover, Germany

[4] Department of Earth Sciences, Natural History Museum, Cromwell Road, London SW7 5BD, UK

Correspondence to: Regina Katsman (rkatsman@univ.haifa.ac.il)

Matthias Halisch (Matthias.Halisch@leibniz-liag.de)

Keywords: multi-methodological approach, permeability, petrography, petrophysics, 3D imaging, pore-scale modelling, upscaling, benchmark study

https://doi.org/10.5194/se-2020-47
Preprint. Discussion started: 4 May 2020

Solid Earth Discussions

Abstract

This paper presents a detailed description and evaluation of a multi-methodological petrophysical approach for the comprehensive multiscale characterization of reservoir sandstones. The suggested methodology enables the identification of Darcy-scale permeability links to an extensive set of geometrical, textural and topological rock descriptors quantified at the pore scale. This approach is applied to the study of samples from three consecutive sandstone layers of Lower Cretaceous age in northern Israel. These layers differ in features observed at the outcrop, hand specimen, petrographic microscope and micro-CT scales. Specifically, laboratory porosity and permeability measurements of several centimetre-sized samples show low variability in the quartz arenite (top and bottom) layers but high variability in the quartz wacke (middle) layer. The magnitudes of this variability are also confirmed by representative volume sizes and by statistical anisotropy analyses conducted on micro-CT-imaged 3D pore geometries. Two scales of porosity variability are revealed by applying variogram analysis to the top layer: fluctuations at 150 μm are due to variability in the pore size, and those at 2 mm are due to the occurrence of high- and low-porosity bands occluded by iron oxide cementation. This millimetre-scale variability is found to control the laboratory-measured macroscopic rock permeability. Good agreement between the permeability upscaled from the pore-scale modelling and the estimates based on laboratory measurements is shown for the quartz arenite (top) layer. The proposed multi-methodological approach leads to an accurate petrophysical characterization of reservoir sandstones with broad ranges of textural, topological and mineralogical characteristics and is particularly applicable for describing anisotropy at various rock scales. The results of this study also contribute to the geological interpretation of the studied stratigraphic units.

https://doi.org/10.5194/se-2020-47
Preprint. Discussion started: 4 May 2020


Solid Earth Discussions

1. Introduction

Permeability is an effective property of a reservoir rock that varies enormously over a wide range of rock length scales, attributed to a hierarchy of dominant sedimentary depositional features (Norris and Lewis, 1991; Nordahl and Ringrose, 2008; Ringrose and Bentley, 2015). Permeability should thus be properly upscaled through the following sequence of scales (Nordahl and Ringrose, 2008; Ringrose and Bentley, 2015 and references therein): (1) from the pore scale (the micro scale, typically microns to millimetres) to the representative elementary volume of a single lamina (the macro scale, typically millimetres to centimetres, e.g., Wildenschild and Sheppard, 2013; Andrä et al., 2013; Bogdanov et al., 2011; Narsilio et al., 2009); (2) to the scale of geological heterogeneity, e.g., the scale of a stratigraphic column (decimetres to decametres, e.g., Jackson et al. 2003; Nordahl et al. 2005); and (3) to the field scale or the scale of an entire reservoir or aquifer (hundreds of metres to kilometres) (Haldorsen and Lake 1984; Rustad et al., 2008). Pore-scale imaging and modelling enable us to relate macroscopic permeability to basic microscopic rock descriptors (Kalaydjan, 1990; Whitaker, 1986; Cerepi et al., 2002; Haoguang et al., 2014; Nelson, 2009). Therefore, the first stage in the above sequence is crucial for successful upscaling to the final reservoir-scale permeability.

Over the past few decades, pore-scale imaging and flow simulations (Bogdanov et al., 2012; Blunt et al., 2013; Cnudde et al., 2013; Wildenschild and Sheppard, 2013; Halisch, 2013) have started to serve as a reliable method for rock characterization. The advantages of these techniques are their non-destructive character and their capability to provide reliable information about the real pore-space structure and topology of rocks. However, despite its importance, the upscaling from the pore scale is sometimes omitted; as a result, effective petrophysical rock characteristics (e.g., porosity and permeability) are often evaluated at the macro scale through only conventional laboratory experiments, which often suffer from errors due to local heterogeneities or a small number of samples (e.g., Halisch, 2013).

The present paper provides a detailed description and evaluation of a multi-methodological petrophysical approach for the comprehensive multiscale characterization of reservoir sandstones. The proposed approach includes petrography, gas porosimetry and permeametry, mercury intrusion porosimetry, 3D imaging and several kinds of pore-scale modelling. The suggested computational workflow enables the identification of Darcy-scale permeability links to an extensive set of geometrical, textural and topological

https://doi.org/10.5194/se-2020-47
Preprint. Discussion started: 4 May 2020

rock descriptors, quantified at the pore scale by deterministic and probabilistic (statistical) methods. Ultimately, this approach is applied to the study of three different consecutive sandstone layers of Lower Cretaceous age in northern Israel.

The approach presented herein is especially important for the detection of anisotropy and the identification of its origin at various rock scales. The multi-methodological validation procedure is significant for properly upscaling permeability from the micro scale to the macro scale (Ringrose and Bentley, 2015). This validation, thereby, allows an accurate petrophysical analysis of reservoir sandstones with broad ranges of textural and topological characteristics. The findings contribute also to the current geological knowledge regarding non-marine sandstones of Lower Cretaceous age (e.g., Akinlotan, 2017; Li et al., 2016; Ferreira et al., 2016) and specifically regarding the studied stratigraphic unit.

2. Geological setting

The study is based on samples collected from a steep outcrop at Wadi E'Shatr near Ein Kinya on the southern slopes of Mt. Hermon (Fig. 1). The outcrop consists of sandstones from the Lower Cretaceous Hatira Formation (Sneh and Weinberger, 2003). This formation (Fm.) acts as a reservoir rock for hydrocarbons in Israel (Fig. 1a), both onshore, namely, Heletz (Grader and Reiss, 1958; Grader, 1959; Shenhav, 1971), and offshore, namely, Yam Yafo (Gardosh and Tannenbaum, 2014; Cohen, 1971; Cohen, 1983; Calvo, 1992; Calvo et al., 2011).

The Hatira Fm. is the lower part of the Kurnub Group of Lower Cretaceous (Neocomian – Barremian) age. The Kurnub Group in the study area (Fig. 1b, d) consists of a volcanic sequence at its base that is overlain with an angular uncomformity by sandstone and clay layers of the Hatira Fm.; the upper unit consists of limestone, marl and chalk – the Nabi Said Fm. (Sneh and Weinberger, 2004). At the section of Saltzman (1967), which is approximately 100 m SW of the sampling area of the present study, the 58 m thick variegated sandstone is interbedded with layers of clay and clay-marl. The sandy component is white-yellow-brown/red and consists of largely angular, poorly sorted, fine- to coarse-grained quartz sand. Individual sandstone layers are cemented by Fe-ox. The outcrops show lenticular benches 0.2 m -1.0 m thick. The clay-rich interlayers are grey and normally siltic and brittle. Locally, these layers contain lignite.

https://doi.org/10.5194/se-2020-47
Preprint. Discussion started: 4 May 2020

The wider geological context of the Hatira Fm. is presented in Appendix A. The outcrop investigated and the specific beds sampled in the present study are shown in Figure 1c.

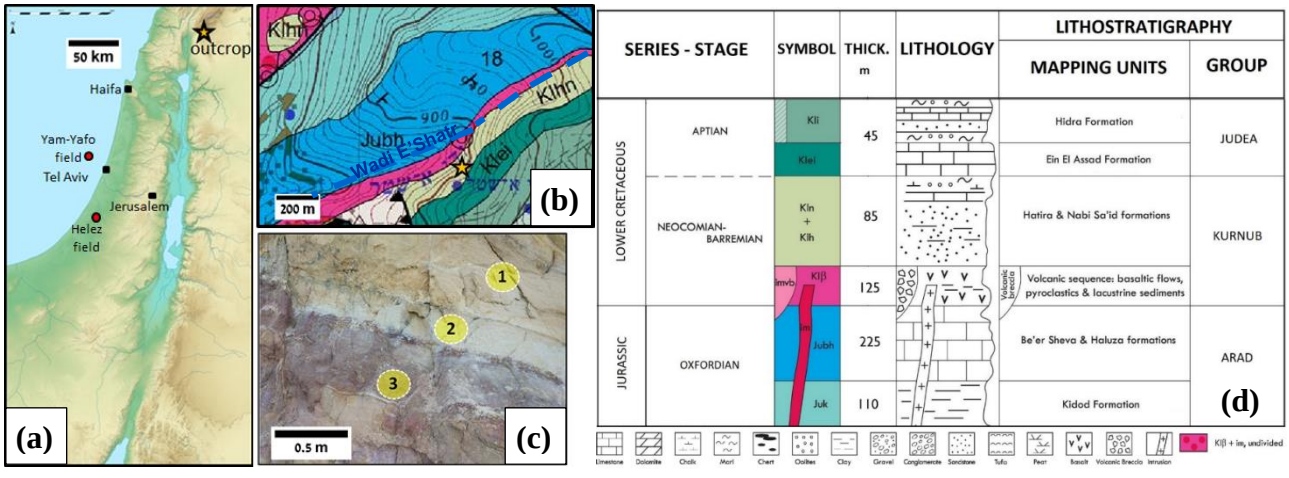

Figure 1: *Geographical and geological settings. (a) Schematic relief map of Israel. The site of Ein Kinya on the southern flanks of Mt. Hermon is indicated by a star (modified from www.mapsland.com). (b) Geological map of Ein Kinya. The Hatira Fm. sandstone and the overlying limestone and marl of the Nabi Said Fm. are marked as Klhn (map is adopted from Sneh and Weinberger, 2014). (c) Outcrop of the* Lower Cretaceous *Hatira Fm. sandstones (Klhn) at Ein Kinya. The studied sandstone layers have distinct colours: yellow-brown (1), grey-green (2), and red-purple (3). (d) Stratigraphic table of the geological map (modified from Sneh and Weinberger, 2014).*

3. Methods

3.1. Sample description

Samples were extracted from three consecutive layers of different colours from a stratigraphic sequence (Figs. 1c, 1d). The lower layer (3) is ~1.5 m thick and consists of sandstone that is light (pale) red-purple in colour with undulating bedding planes between the sub-layers. The middle layer (2) is composed of grey – green shaly sandstone that is 20 cm thick with dark horizons at the bottom and top. The upper layer

https://doi.org/10.5194/se-2020-47
Preprint. Discussion started: 4 May 2020


Solid Earth Discussions

(1) comprises 1.5 m thick homogenous brown-yellow sandstone. Large sample blocks were collected from these three layers, and the directions perpendicular to the bedding planes (defined as the z-directions in our study) were noted. Subsequently, in the laboratory, smaller sub-samples (described below) were prepared from these large samples for textural observations and various analytical measurements and computations. In total, 7 sub-samples from the top layer, 8 sub-samples from the middle layer and 4 sub-samples from the bottom layer were investigated in the laboratory (Table 2).

3.2. Laboratory and computational methods for rock characterization

The integrated analytical programme designed for this study includes the following laboratory measurements and computations conducted at different scales (from the micro scale reflecting the scale of individual pores and grains to the core scale reflecting the scale of the laminas at the outcrop) (Table 1). Specimens ~5-7 cm in size were investigated by petrographic and petrophysical lab methods. Sub-samples ~1 cm in size were retrieved from the aforementioned plugs for investigation by 3D imaging, digital image analysis and simulation techniques (described in more detail below).

Table 1. *Laboratory methods employed and petrophysical characteristics determined in this study*

Method	**Determined petrophysical characteristics**
1. Scanning electron microscopy (SEM)	Mineral abundance, grain surface characterization of matrix and cementation
2. Grain size analysis (Laser diffraction)	Grain size distribution (*GSD*)
3. X-ray diffraction (XRD)	Mineral components
4. Nitrogen gas porosimetry	Porosity (ϕ)
5. Steady state permeametry	Permeability (1D) (κ)
6. Mercury intrusion porosimetry (MIP)	Pore throat size distribution (*PTSD*), specific surface area (*SSA*), characteristic length (l_c), pore throat length of maximal conductance (l_{max}), permeability (κ)
7. Petrographic microscopy Plane-parallelized (PPL) and cross-parallelized (XPL) and reflected-light (RL) microscopy, binocular (BINO).	Mineral abundance, grain surface characterization, cementation

https://doi.org/10.5194/se-2020-47
Preprint. Discussion started: 4 May 2020

8. Extended computational workflow:	
Digital image analysis (DIA)	Porosity (ϕ), pore specific surface area (*PSA*), tortuosity (τ), pore size distribution (*PSD*), connectivity index (*CI*), micro-CT predicted porosity from MIP
Fluid flow modelling	Permeability tensor ($\bar{\bar{\kappa}}$), tortuosity (τ)

Petrographic descriptions of rock compositions and textures at the micro scale, notably those of the fine fraction, were performed using scanning electron microscopy (*JCM-6000 Bench Top SEM device*, Krinsley et al., 2005) using both backscatter and secondary electron modes.

Thin-section optical microscopy (*Olympus BX53 device*, Adams et al., 2017) was used to estimate the mineral abundance and surface features of the grains, and the mineralogical and textural features of matrix and cement. Grain size distributions were determined by a laser diffraction particle size analyser (LS 13 320). X-ray diffraction (*Miniflex 600 device by Rigaku*) was applied to powdered samples to determine their mineralogical composition.

Effective porosity and permeability were evaluated on dried cylindrical samples (2.5 cm in diameter and 5-7 cm in length) following the RP40 guidelines (*Practices for Core Analysis, API, 1998*). Effective porosity (ϕ) was measured using a steady-state nitrogen gas porosimeter produced by Vinci Technologies (*HEP-E, Vinchi Technology,* v3.20). Absolute permeability (κ) was measured by using a steady-state nitrogen gas permeameter (*GPE, Vinci Technologies*; e.g., Tidwell and Wilson, 1999).

Mercury intrusion porosimetry (*Micromeritics AutoPore IV 9505*, which considers pore throats larger than 0.006 μm) was applied to dried cylindrical samples ~1 cm^3 in size to evaluate the following parameters (Table 1):

- Pore throat size distribution (*PTSD,* Lenormand, 2003).
- Specific surface area (*SSA*): the pore surface to bulk sample volume (Rootare and Prenzlow, 1967; Giesche, 2006).
- Characteristic length (l_c): the largest pore throat width (obtained from the increasing intrusion pressure) at which mercury forms a connected cluster (Katz and Thompson, 1987).

https://doi.org/10.5194/se-2020-47
Preprint. Discussion started: 4 May 2020

- Pore throat length of maximal conductance (l_{max})*:* defines a threshold for the pore throat size l at which all connected paths composed of $l \geq l_{max}$ contribute significantly to the hydraulic conductance, whereas those with $l < l_{max}$ may completely be ignored (Katz and Thompson, 1987).
- Permeability (Katz and Thompson, 1987):

$$\kappa = \frac{1}{89} l_{max}^2 \frac{l_{max}}{l_c} \phi S(l_{max}) \quad (1)$$

where $S(l_{max})$ is the fraction of connected pore space that is composed of pore throat widths of size l_{max} and larger. This approach (Katz and Thompson, 1987), which was derived from percolation theory (Ambegaokar et al., 1971), is applicable for sandstones with a broad distribution of local conductances with short-range correlations only.

An extended computational workflow (similar to the procedure presented by Boek and Venturoli, 2010; Andrä et al., 2013) (Fig. 2) serves as one of the main methodologies in our study to upscale permeability. It includes 3D micro-CT imaging of porous samples, digital image processing and segmentation, statistical analyses for the determination of representative elementary volumes, and pore-scale flow modelling through the 3D pore geometry of the rock. First, cylindrical subsamples 4-8 mm in diameter and 5-10 mm in length were retrieved from the larger samples studied in the laboratory and were scanned non-destructively (Fig. 2b) by using a *Nanotom* 180 S micro-CT device (*GE Sensing & Inspection Technologies, phoenix|X-ray product line*, Brunke et al., 2008). The achieved voxel size of the data sets was 2.5 µm (isotropic), suitable for imaging pore throats that effectively contribute to the flow in the studied type of sandstone (e.g., Nelson, 2009). Afterwards, all data sets were filtered for de-noising, X-ray artefact removal and edge enhancement (Fig. 2c). The post-processed images had an edge length of 1180 voxels or 2950 µm. Image artefacts were processed as described by Wildenschild and Sheppard (2013). Beam hardening artefacts were removed by applying the best-fit quadratic surface algorithm (Khan et al., 2016) to each reconstructed 2D slice of the image. Ring artefact reduction and image smoothing (with preservation of sharp edge contrasts) were performed using a non-local means filter (Schlüter, 2014). Segmentation was performed to convert the grey-scale images obtained after image filtering into binary images to distinguish between voids and solid phases (Fig. 2c). The local segmentation approach, which considers the spatial dependence of the intensity for the determination of a voxel phase, was used in addition to a histogram-based

https://doi.org/10.5194/se-2020-47
Preprint. Discussion started: 4 May 2020


Solid Earth
Discussions
Open Access
EGU

183 approach (Iassonov et al., 2009; Schlüter et al., 2014). Two-phase segmentation was performed by the
184 converging active contours algorithm (Sheppard et al., 2004), a combination of a watershed (Vincent et al.,
185 1991) with an active contour algorithm (Kass et al., 1988).

186

https://doi.org/10.5194/se-2020-47
Preprint. Discussion started: 4 May 2020

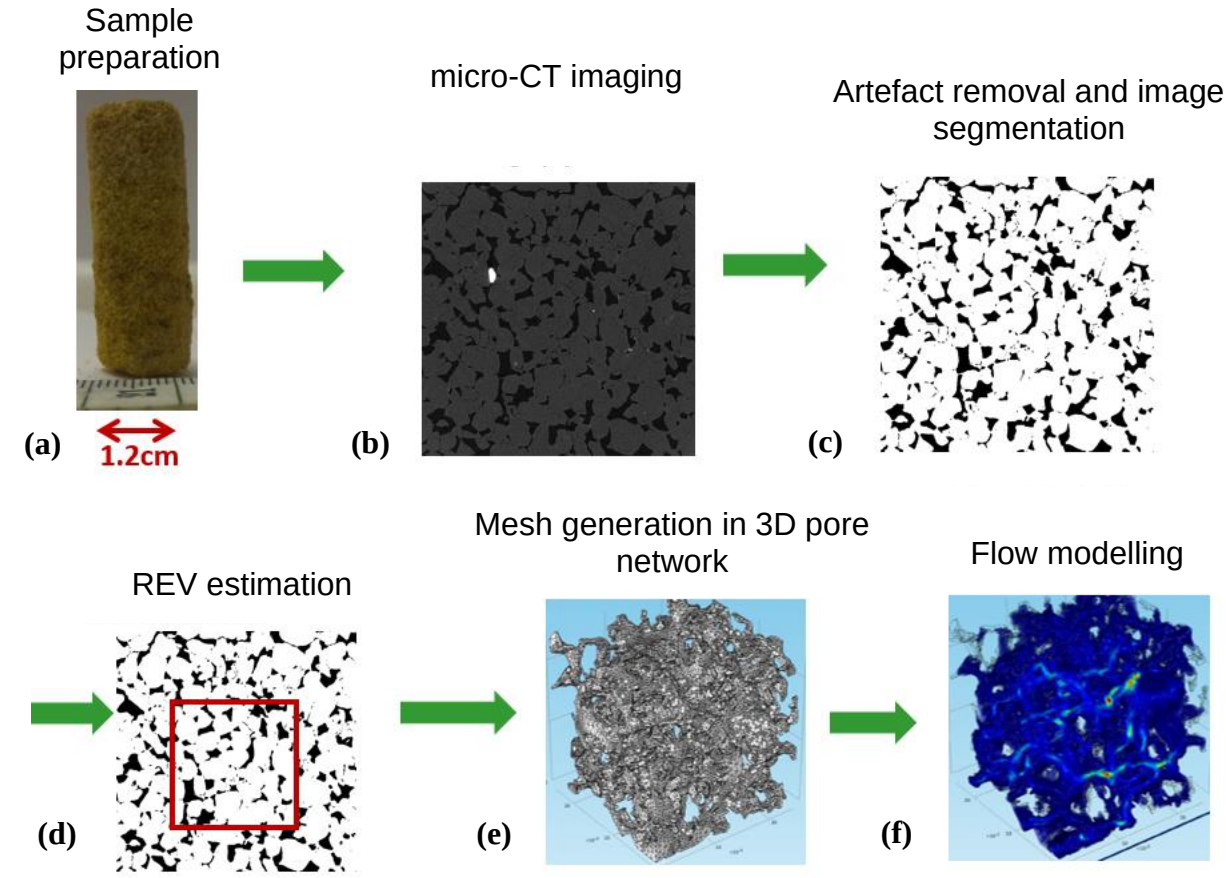

Figure 2. *Extended computational workflow. See text for more details. Images* ***(e)*** *and* ***(f)*** *are adopted from Bogdanov et al. (2012).*

Simulations involving the real geometry of an imaged rock are computationally power and time consuming. Therefore, the determination of a representative elementary volume (REV) is required (Fig. 2d), assuming that porous media are homogeneous at REV dimensions (Bear, 1988). An REV is required in the current study to perform fluid flow simulations. Porosity, a basic macroscopic structural property of porous media, is used here for the estimation of an REV (Bear, 1988; Halisch, 2013; Tatomir et al., 2016) based on its correlation with permeability (Kozeny, 1927; Carman, 1956).

Two approaches were used in this study to estimate the REV (Halisch, 2013). In the "classic" approach, the REV is attained when porosity fluctuations in the sub-volumes that grow isotropically in three

https://doi.org/10.5194/se-2020-47
Preprint. Discussion started: 4 May 2020


Solid Earth Discussions

orthogonal directions become sufficiently small (Bear, 1988). Practically, a large number of randomly distributed cubes were analysed through the entire 3D sample (with a 1180 voxel edge length in our case) for their image porosity (IP). The chosen initial cube size (with an edge length of 10 pixels in our case) was increased by 10-100 voxels. The REV size was specified when agreements between the mean and median IP values as well as saturation in the IP fluctuations were attained. The results of the REV estimation by this classic approach can be found in Appendix B.

A more advanced "directional" REV approach can capture porosity changes in a specific direction caused by microscopic structural features, such as grain packing, cracks, and textural effects (Halisch, 2013). The average porosity is first calculated slice by slice across the segmented image in each orthogonal direction. Variogram analysis (Cressie, 1993) is used to describe the degree of spatial variability of the porosity in each direction based on the assumption that a distance at which no spatial correlation exists reflects the scale of homogeneity, which defines the REV. The variogram $\hat{\gamma}(h)$, i.e., the expected squared difference between two observations (here, the average of 2D IPs), is calculated as a function of their separation distance, *h (lag)*. Practically, the lag distance at which the variogram curve is saturated is the distance at which no spatial correlation exists (defined as the range of a spatial correlation). Depending on the sample heterogeneity at different scales, the variogram may manifest a different range for each scale. Variogram analysis was performed using the 'Variogramfit' MATLAB package.

Further, the representative binary 3D image (REV) of the pore space was spatially discretised by tetrahedrals with *Materialize software (Belgium)* (Fig. 2e). This step is required for importing the REV into the FEM-based modelling software (*Comsol Multiphysics simulation environment*, v5.2a). Stokes flow (Re << 1) is simulated (Table 1) in the pore network (Fig. 2f) by the following equations (e.g., Narsilio et al., 2009; Bogdanov et al., 2011):

Stokes equation: $$-\nabla p + \mu \nabla^2 \bar{u} = 0 \quad (2)$$

Continuity equation: $$\nabla \cdot \bar{u} = 0 \quad (3)$$

where ∇p is the local pressure gradient, $\bar{u}$ is the local velocity vector in the pore space and μ is the dynamic fluid viscosity. Fixed pressures (*p=const*) were specified at the inlet and outlet boundaries of the fluid domain. At the internal pore walls and at the lateral domain boundaries, no-slip boundary conditions ($\bar{u} = 0$) were imposed (e.g., Guibert et al., 2014). These also simulate the flow setup in a steady-state experimental

https://doi.org/10.5194/se-2020-47
Preprint. Discussion started: 4 May 2020


Solid Earth Discussions

permeameter (e.g., Renard et al., 2001). The macroscopic fluid velocity $< \bar{v} >$ was evaluated by volumetrically averaging the local microscopic velocity field (e.g., Narsilio, 2009; Guibert et al., 2016). Then, from the average macroscopic velocity vectors v_i^j in three orthogonal *i*-directions corresponding to the pressure gradients ∇p_j imposed in *j*-directions, the full 3D second-rank upscaled permeability tensor $\bar{\bar{\kappa}}$ can be found:

$$\begin{pmatrix} v_x^x & v_x^y & v_x^z \\ v_y^x & v_y^y & v_y^z \\ v_z^x & v_z^y & v_z^z \end{pmatrix} = -\frac{1}{\mu\phi}\begin{pmatrix} \kappa_{xx} & \kappa_{xy} & \kappa_{xz} \\ \kappa_{yx} & \kappa_{yy} & \kappa_{yz} \\ \kappa_{zx} & \kappa_{zy} & \kappa_{zz} \end{pmatrix}\begin{pmatrix} \nabla p_x & 0 & 0 \\ 0 & \nabla p_y & 0 \\ 0 & 0 & \nabla p_z \end{pmatrix} \quad (4)$$

The permeability tensor is symmetrized by:

$$\bar{\bar{\kappa}}_{sym} = \frac{1}{2}(\bar{\bar{\kappa}} + \bar{\bar{\kappa}}^T) \quad (5)$$

Tortuosity (τ; Bear, 1988; Boudreau, 1996) was calculated separately in the x-, y- and z-directions in the meshed domain using the particle tracing tool of *Comsol Multiphysics software* (an additional method for deriving τ is presented later in this section).

3D image analysis (Table 1) was conducted on a high-quality, fully segmented micro-CT image (edge length of 2950 µm scanned at a 2.5 µm voxel size). Non-connected void clusters in the binary specimen were labelled and then separated into objects (single pores and grains) by using a distance map followed by the application of a watershed algorithm (e.g., Brabant et al., 2011; Dullien, 2012). Image analysis operations were assisted by *Fiji-ImageJ software* (Schindelin et al., 2012) and by the *MorphoLibJ plug-in* (Legland et al., 2014). The following geometrical descriptors were derived from the segmented image limited by the image resolution of 2.5 µm (Table 1):

- micro-CT image porosity (*IP*);
- Pore specific surface area (*PSA* – surface to pore volume);
- Tortuosity: evaluated in the x-, y- and z-directions by finding the average of multiple shortest paths through the main pore network using the fast marching method (Sethian, 1996) implemented using an accurate fast marching plug-in in MATLAB.
- Pore size distribution *(PSD)*: obtained by a Feret maximum calliper (Schmitt et al., 2016).

https://doi.org/10.5194/se-2020-47
Preprint. Discussion started: 4 May 2020

- Euler characteristic (χ) - a topological invariant (Wildenschild and Sheppard, 2013; Vogel, 2002) that describes the structure of a topological space (see Appendix C for more detail). Since the number of pore connections depends on the number of grains, it is essential to normalize χ (Scholz et al., 2012) to compare the connectivity among three samples that have the same dimensions but different grain sizes.
- Connectivity index (*CI*): computed by dividing the absolute value of the Euler characteristic ($|\chi|$) by the number of grains in the specimen (N, determined by image analysis), $CI = |\chi|/N$.

Additionally, we propose a simple and new method to estimate the image porosity at a given resolution. Multiplication of the mercury effective saturation at the capillary pressure corresponding to the micro-CT resolution (i.e., 2.5 µm) by the porosity of the same sample measured by a gas porosimeter yields the *micro-CT-predicted image porosity from MIP* at the given resolution limit (Table 1).

https://doi.org/10.5194/se-2020-47
Preprint. Discussion started: 4 May 2020


Solid Earth Discussions

263 ## 4. Results

264 ### 4.1. Petrographic and petrophysical rock characteristics

265 Three types of sandstone rocks were characterized by techniques 1-8 listed in Table 1. The results are
266 presented in Figures 3-8 and summarized in Table 2.

267 **Sandstone S1**: The top unit layer with a thickness of ~1.5 m (Fig. 1c) consists of yellow-brown
268 sandstone (Fig. 3a), which is moderately consolidated. The sandstone is a mature quartz arenite (following
269 Pettijohn et al., 1987) with minor Fe-ox, feldspar and heavy minerals. The grain size distribution has a mean
270 of ~325 μm (Fig. 6a, Table 2). The grains are moderately sorted (according to the classification of Folk and
271 Ward, 1957) and sub-rounded to well-rounded with local thick (millimetre-scale), relatively dark envelopes
272 (Fig. 3b). The sandstone consists of alternating millimetre-scale layers of large and small sand grains.
273 Secondary silt (~ 45 μm) and clay (~0.95 μm) populations are detected in the grain size distribution (Fig. 6).
274 X-ray diffraction detected a small amount of kaolinite. The Fe-ox grain-coating and meniscus-bridging
275 cement is composed of overgrown flakes aggregated into structures ~10 μm in size (Fig. 3c-3f). Mn-ox is
276 also evident but is scarce (Fig. 3e).

277 The pore network is dominated by primary inter-granular well-interconnected macro porosity (Fig.
278 3b). However, sealed and unsealed cracks in grains are also observed. Higher Fe-ox cementation at the
279 millimetre scale on horizontal planes is recognized (Fig. 3a). In addition, smaller voids between Fe-ox
280 aggregates and flakes occur at the micrometre scale and smaller (Fig. 3d-f).

281 The pore throat size analysis conducted with MIP shows that 82 % of the pore volume is composed of
282 macro pores (>10 μm) following a log-normal distribution with a peak at 44 μm (Fig. 7a). The characteristic
283 length, i.e., the largest pore throat length at which mercury forms a connected cluster, is $l_c = 42.9$ μm (Fig.
284 7b), and the pore throat length of maximal conductance is $l_{max} = 34.7$ μm (Appendix D, Fig. D1). The
285 porosity evaluated by laboratory gas porosimetry varies in the range of 26-29 % for 7 different samples of
286 S1 (Fig. 8). Multiplying the mercury effective saturation (85.8 %) at the micro-CT resolution (2.5 μm) (Fig.
287 7a, red dashed line) by the porosity of the same sample measured by gas porosimetry (27.3 %) yields a
288 micro-CT-predicted image porosity of 23.5 % at a resolution limit of 2.5 μm (Table 2).

https://doi.org/10.5194/se-2020-47
Preprint. Discussion started: 4 May 2020

Solid Earth
Discussions
Open Access
EGU

289 The permeability evaluated by a laboratory gas permeameter has averages of 350 mD (range of 130-
290 500 mD) for 5 samples measured perpendicular to the depositional plane (z-direction) and 640 mD for 2
291 samples measured parallel to the depositional plane (x- and y-directions) (Fig. 8). MIP measurement (Katz
292 and Thompson, 1987) yields a permeability (see Sect. 3.2) of 330 mD (Table 2).

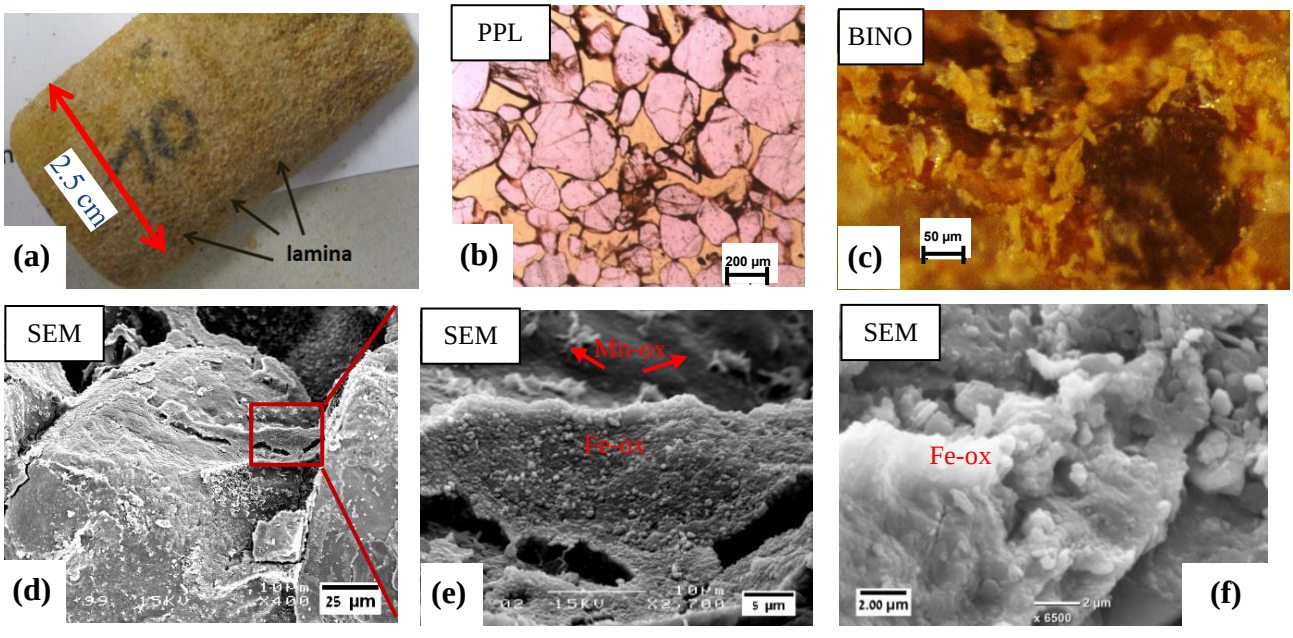

293

294

295

296 ***Figure 3:*** *Representative images of sandstone S1.* ***(a)*** *Darker laminae in the x-y plane at the millimetre scale*
297 *are observed.* ***(b)*** *Thin section image of S1: quartz grains are shown in pink, while pores are in yellow.* ***(c)***
298 *Fe-ox flakes (yellow) on quartz grains (pale grey) identified with binocular.* ***(d)*** *SEM image of S1: grain-*
299 *coating, meniscus-bridging cement and overgrowth of Fe-ox flakes are observed. Magnified images at*
300 *different scales are presented in* ***(e)-(f)****.*

301

https://doi.org/10.5194/se-2020-47
Preprint. Discussion started: 4 May 2020

302 ***Table 2.*** *Petrophysical characteristics of the three studied sandstone layers.*

	Method	S1	S2	S3
Grain size	Laser diffraction	325 µm **medium sand** **moderately sorted** sand: 92.6 % silt: 6.6 % clay: 0.8 %	154 µm **very fine sand** **poorly sorted** 65.7 % 31.3 % 3 %	269 µm **fine sand** **moderately sorted** 94.4 % 4.8 % 0.8 %
Pore throat size	MIP	Mode 1: 44 µm Mode 2: 0.035 µm Mode 3: 2.2 µm **macro pores** **well sorted**	0.035 µm 3.5 µm **meso pores** **poorly sorted**	35 µm 0.035 µm 2.2 µm **macro pores** **well sorted**
Pore size	Image analysis (min. object size 2.5 µm)	194 µm (*FWHM [150,335] µm)	Mode 1: 21 µm Mode 2: ~100 µm	223 µm (*FWHM [145,400] µm)
Characteristic length, l_c	MIP	42.9 µm	12.3 µm	36.9 µm
l_{max} contributing to maximal conductance	MIP	34.7 µm	8 µm	31.4 µm
Porosity, ϕ	Gas porosimetry	28 ± 2 % (7**)	19 ± 5 % (8)	31 ± 1 % (4)
	CT predicted image porosity from MIP	23.5 %	6.6 %	30.4 %
	Micro-CT segmented	17.5 %	6.9 %	28.3 %
Permeability, κ ⊥ - perpendicular to layering (z-direction) || - parallel to layering (x-y plane)	Gas permeametry	⊥ 350 mD (5) || 640 mD (2)	⊥ 2.77 mD (5) || 7.73 mD (3)	⊥ 220 mD (2) || 4600* mD (2)
	MIP	330 mD (1)	4 mD (1)	466 mD (3)
	Flow modelling	$\begin{pmatrix} 420 & 66.3 & 1.91 \\ 66.3 & 344 & 12.8 \\ 1.91 & 12.8 & 163 \end{pmatrix}$ mD	-	$\begin{pmatrix} 4517 & 5 & 38 \\ 5 & 4808 & 547 \\ 38 & 547 & 4085 \end{pmatrix}$ mD
Specific surface area, *SSA* (surface-to- bulk-volume)	MIP	3.2 μm^{-1}	12.2 μm^{-1}	0.16 μm^{-1}
Pore specific surface area, *PSA* (surface-to-pore-volume)	Micro-CT at 2.5 µm resolution size	0.068 μm^{-1}	0.136 μm^{-1}	0.069 μm^{-1}
Connectivity index	Image analysis	3.49	0.94	10
Tortuosity, τ	Flow modelling	-	-	x: 1.443 y: 1.393 z: 1.468
	Micro-CT shortest path analysis	x: 1.385 y: 1.373 z: 1.477	-	x: 1.316 y: 1.338 z: 1.394

303 Legend:

https://doi.org/10.5194/se-2020-47
Preprint. Discussion started: 4 May 2020

304 *Addressed in the Discussion.
305 ** Numbers in parentheses related to gas porosity, gas permeability and MIP permeability indicate the
306 number of plugs for the measurements. Other measurements and calculations were conducted on single
307 plugs.
308 FWHM - full width at half maximum, log-normal distribution.
309

310 **Sandstone S2**: The intermediate unit layer with a thickness of ~20 cm consists of grey-green
311 moderately consolidated sandstone (Figs. 1c, 4) composed of sub-rounded to rounded, very fine sand grains
312 (~154 μm); the sandstone is poorly sorted with 35 % of the particles being silt and clay (Fig. 6, Table 2).
313 Secondary silt (~ 40 μm), sand (~400 μm) and clay (~1.5 μm) populations are also detected. The grains are
314 composed of quartz with minor Fe-ox coating the grains and minor quantities of heavy minerals (Fig. 4c).
315 Clay filling the pore space was identified by XRD as a kaolinite mineral. It appears as a grain-coating,
316 meniscus-bridging, and pore-filling matrix (Fig. 4b, c). Therefore, the unit layer (Fig. 1c) is classified as a
317 quartz wacke sandstone.

318 The pore network is influenced by the extent of clay deposition on coarser grains, identified mostly in
319 laminae (Fig. 4a, d). However, the inter-granular connectivity of macro pores can still be recognized (Fig.
320 4b, c). The effective pore network consists of inter-granular macro pores distributed between the laminae or
321 zones richer in clay and Fe-ox. Integrating the grain size and pore throat size analysis results (Figs. 6, 7)
322 confirms that the reduction in the inter-granular pore space in S2 is due to the clay matrix, which is reflected
323 in the poor grain sorting and large variance in pore size. In the pore throat size analysis (Fig. 7), only 15 %
324 of the pore volume is composed of macro pores that are larger than 10 μm. The prominent sub-micron pore
325 mode is ~35 nm, with a population containing ~45 % of the pore volume (Fig. 7a). This population of pores
326 occurs inside the clay matrix. The secondary pore volume population is poorly distributed within the range
327 of 0.8-30 μm. The characteristic length (Sect. 3.2), $l_c = 12.3$ μm (Fig. 7b), and the pore throat length of
328 maximal conductance, $l_{max} = 8$ μm (Appendix D, Fig. D1) (both have a large uncertainty resulting from
329 uncertainty in the threshold pressure), suggest a connectivity of macro pores regardless of their small
330 fraction within the total pore space. The porosity of S2 evaluated for 8 different samples varies in the range
331 of 14.5-23.5 % (Fig. 8). From the *PTSD* (Table 1) and gas porosimetry results (for a sample with a porosity
332 of 18.6 %), micro-CT predicts an image porosity of 6.6 % at a resolution limit of 2.5 μm (Table 2). The gas

https://doi.org/10.5194/se-2020-47
Preprint. Discussion started: 4 May 2020

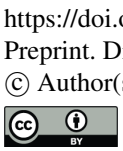

permeability in the z-direction was measured in 5 samples (Fig. 8): in four of them, the permeability ranges within 1-12 mD and increases with porosity. However, one sample had an exceptionally large porosity and permeability of 23 % and 62 mD, respectively. The permeability measured for 3 samples in the x-y plane ranges within 4-12 mD, also showing ~15 % porosity (Fig. 8). In addition, for the samples with ~15 % porosity, their permeability is ten times larger in the x-y plane (parallel to the layering) than in the z-direction (perpendicular to the layering). The permeability derived from MIP reaches 4 mD, which agrees with an average of 2.77 mD and 7.73 mD (Table 2) measured in the z-direction with a gas permeameter (excluding one exceptionally high value, Fig. 8).

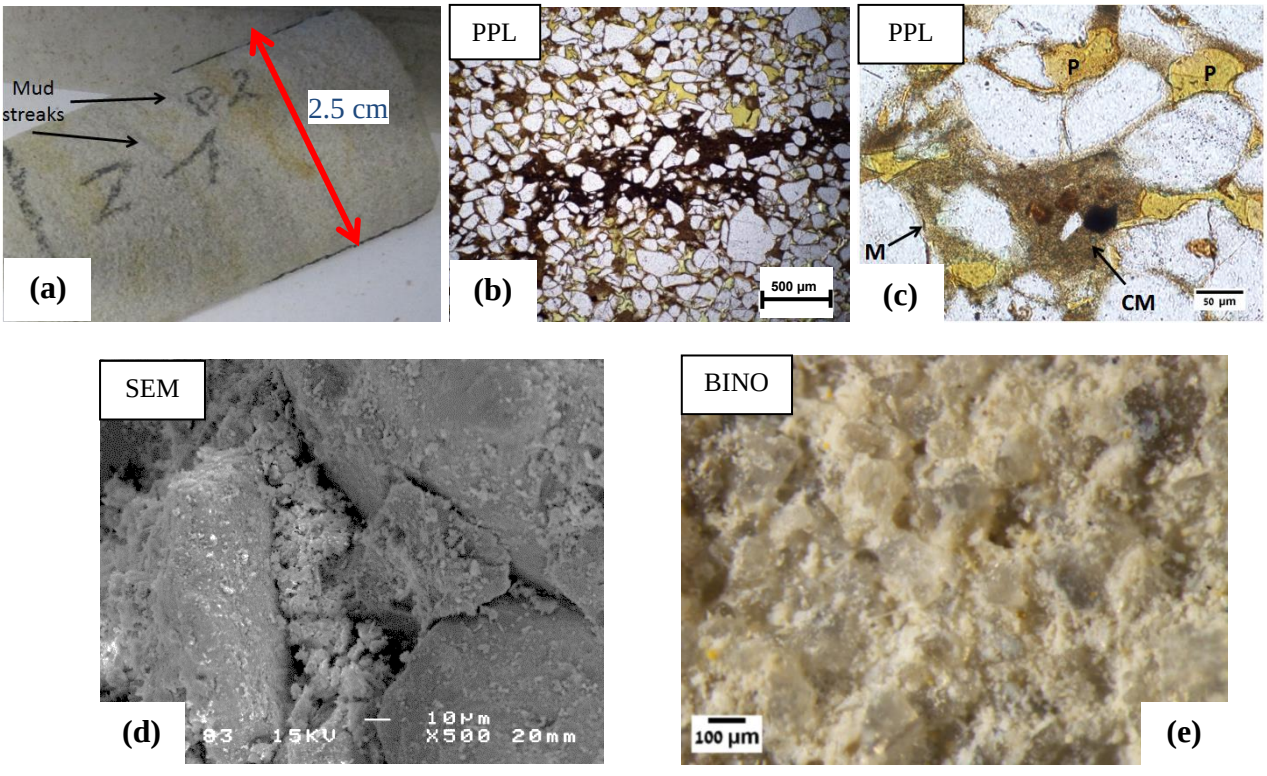

Figure 4. *Representative images of sandstone S2.* ***(a)*** *Prominent dark and yellowish zones are observed.* ***(b)*** *The dark laminae are richer in clays and Fe-ox.* ***(c)*** *Clay and silt accumulated as meniscus (M) and as clay matrix (CM). P refers to open pores.* ***(d)*** *Pore clogged by clay and Fe-ox.* ***(e)*** *Rock texture under binocular. The clay matrix is white, and quartz grains are pale grey.*

https://doi.org/10.5194/se-2020-47
Preprint. Discussion started: 4 May 2020

Sandstone S3: Samples were taken from the ~1.5 m thick bottom unit layer in the outcrop (Fig. 1c) consisting of (pale) red-purple poorly consolidated sandstone with grains covered by a secondary red patina (Fig. 5). The sandstone is composed of friable to semi-consolidated, fine (~269 µm), moderately sorted sand (Table 2), where only 5.6 % of particles are silt and clay (Fig. 6). Secondary silt (~ 50 µm) and clay (~ 0.96 µm) populations were also detected. The sandstone consists of sub-rounded to rounded grains showing a laminated sedimentary texture consisting of the cyclic alternation of relatively dark and light red bands of millimetre-scale thickness (Fig. 5a). The dark laminae contain slightly more Fe-ox meniscus-bridging and pore-filling cementation (Fig. 5b, d). Overall, this bed consists of a ferruginous quartz arenite. The grains are dominated by quartz with very minor feldspar and black opaque mineral grains, perhaps Fe-ox (Fig. 5d). X-ray diffraction indicated quartz only. The Fe-ox coating of grains is less extensive than in other samples (Fig. 5c). The pore interconnectivity in this sandstone is high (Fig. 5d). Heavier cementation is rarely observed (Fig. 5d) and is organized in horizontal laminae (Fig. 5a). Features including grain cracks, grain-to-grain interpenetration, and pressure solution are also recognized (Fig. 5e). The *PTSD* showed that 95 % of the pore volume is presented by macro pores (Fig. 7a), which agrees with the minority of fine particles. The characteristic length and pore throat length of maximal conductance are $l_c = 36.9$ µm (Fig. 7b) and $l_{max} = 31.4$ µm (Appendix D, Fig. D1), respectively.

The porosity measured by a gas porosimeter in the laboratory varies in the range of 30-32 % for 4 different samples (Fig. 8). From *PTSD* and gas porosimetry (Figs. 7, 8), the micro-CT-predicted image porosity at a resolution limit of 2.5 µm is 30.4 % (Table 2). The permeability measured by a laboratory gas permeameter averages 220 mD for 2 samples measured in the z-direction and 4600 mD for 2 samples measured in the x-y plane (Fig. 8), showing a ten-fold difference (discussed in Sect. 5). The permeability derived from MIP reaches 466 mD (Table 2).

https://doi.org/10.5194/se-2020-47
Preprint. Discussion started: 4 May 2020

370

371

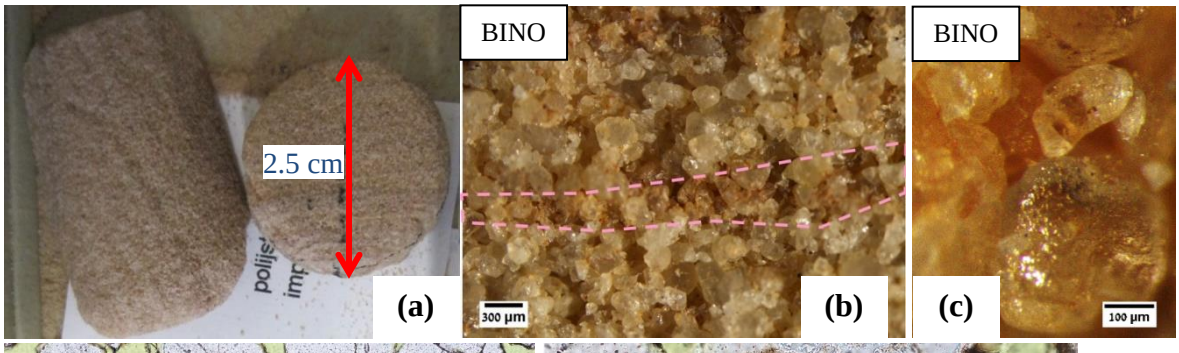

372

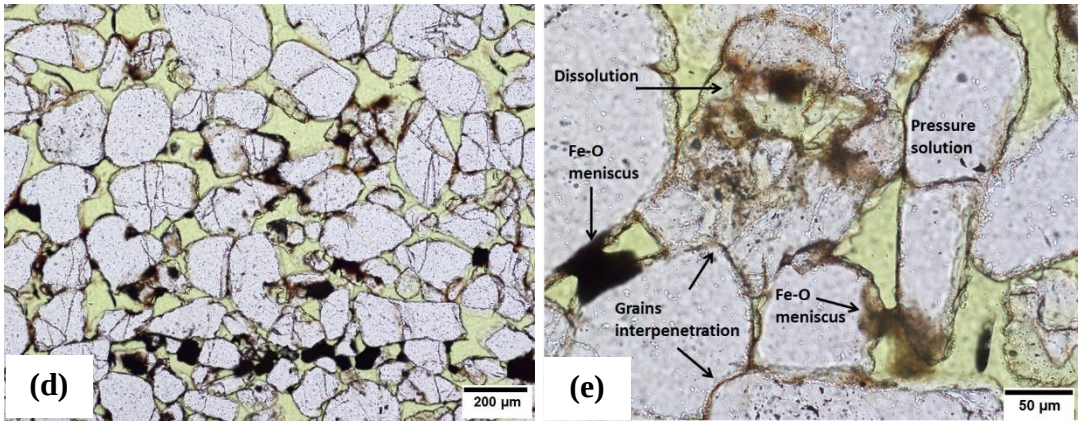

373 ***Figure 5.*** *Representative images of sandstone S3.* ***(a)*** *Laminae are recognized by their slightly dark and red*
374 *colour.* ***(b)*** *General view under a binocular microscope reveals red laminae ~500 µm thick.* ***(c)*** *High-*
375 *resolution observation of a clear grain under binocular.* ***(d)*** *A millimetre-scale lamina is indicated by*
376 *enhanced meniscus-type Fe-ox cementation and partly by inter-granular fill. Grain surfaces are coated by*
377 *thin Fe-ox. Black and orange cements represent crystallized and non-crystallized Fe-ox, respectively. Some*
378 *cracked grains are observed, sporadically cemented by Fe-ox.* ***(e)*** *Partially dissolved grains are coated by*
379 *cement.*

380

https://doi.org/10.5194/se-2020-47
Preprint. Discussion started: 4 May 2020

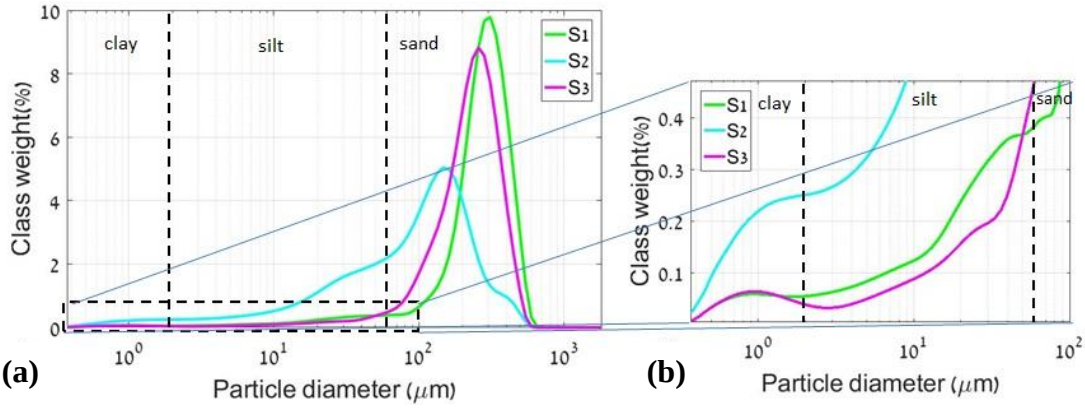

Figure 6: ***(a)*** *Grain size distribution.* ***(b)*** *Magnified grain size distribution in the fine grain size region plotted for sandstones S1 (green), S2 (blue) and S3 (purple). S1 and S3 have a unimodal distribution and are moderately sorted with a small skewness tail. Sample S2 has a multi-modal distribution and is poorly sorted.*

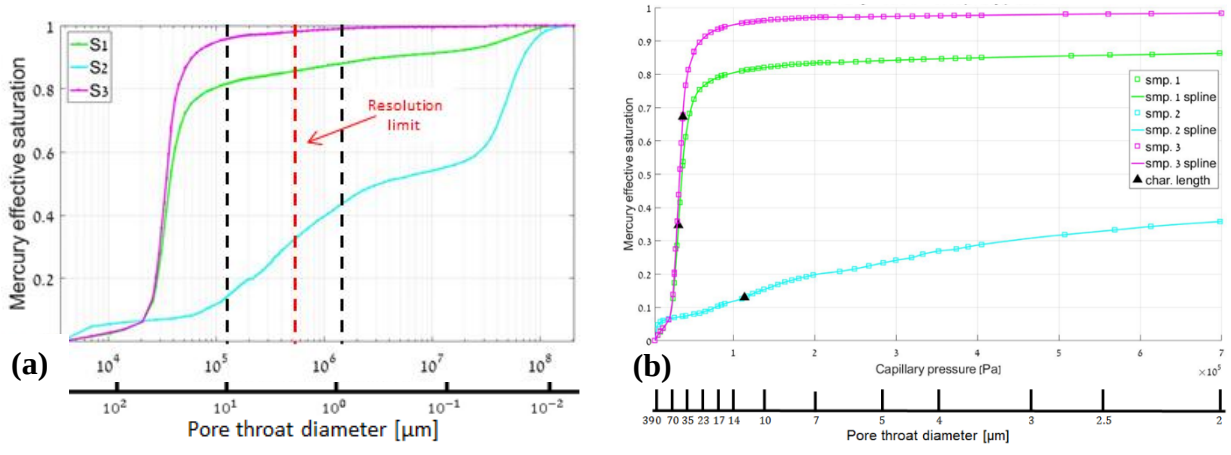

Figure 7: *Cumulative pore throat sizes of the studied sandstones.* ***(a)*** *Capillary pressure on a logarithmic scale. The resolution limit of the micro-CT imaging indicates the fraction of the pore space that could be resolved.* ***(b)*** *Capillary pressure on a normal scale. The triangles indicate the characteristic length, l_c.*

https://doi.org/10.5194/se-2020-47
Preprint. Discussion started: 4 May 2020

389

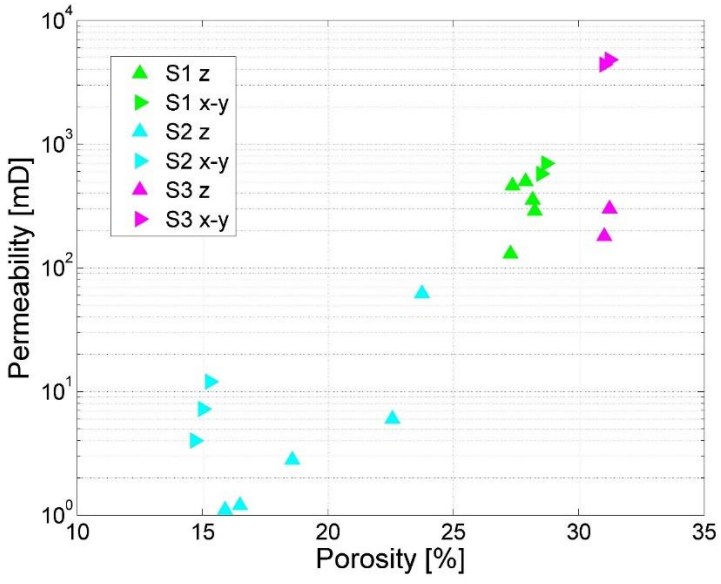

390

391 ***Figure 8:*** *Results of porosity-permeability lab measurements. The permeability of the samples was*
392 *measured in directions perpendicular to the bedding (z-direction) and parallel to the bedding (x-y plane).*

393 Overall, for all three investigated sandstones, the pore throat size contributing to the maximal conductance,
394 l_{max}, is smaller than the characteristic length, l_c (Table 2), when the relative decrease is greater for the
395 layers containing more fines.

396 Additionally, pore surface roughness may be evaluated from the specific surface area (*SSA*) measured
397 by MIP (Table 2). A larger *SSA* implies a rougher surface (e.g., Tatomir et al., 2016). The *SSA*s for S1 and
398 S2 (3.2 μm^{-1} and 12.2 μm^{-1}, respectively) are similar to those given in the literature for sandstones of
399 similar properties (e.g., Cerepi et al., 2002). The *SSA* of S2 is higher because of its high silt and clay content
400 of 34.3 %, which is only 7.4 % for S1 (Fig. 6a). The *SSA* of S3 (where silt and clay constitute only 5.6 %,
401 including the Fe-ox rim coating) is only 0.16 μm^{-1}, which is 20 times smaller than that of S1 (Table 2). The
402 difference in *SSA*s between S1 and S3, which are similar in their grain and pore throat size distributions
403 (Figs. 6, 7), is a result of S1 having a higher Fe-Ox grain coating than S3 (compare Figs. 3d and 5c).

https://doi.org/10.5194/se-2020-47
Preprint. Discussion started: 4 May 2020

In summary, although the S1 pore network has larger pore throats, it also has greater grain roughness and lower connectivity than S3. These two properties dominate and generate a smaller permeability for S1 than for S3 (Table 2).

4.2. REV Analysis

The results of the directional REV analysis of sample S1 conducted on a cube with a 2950 μm edge size (1180 pixels) scanned with a resolution of 2.5 μm are shown in Figures 9 and 10. The average slice-by-slice porosity analysed in three directions distinguishes the z-direction as having an exceptional behaviour (Fig. 9a-c). Specifically, the difference between the maximum and minimum porosities is 7.44 % in the z-direction (in contrast to 5.7 % in the x- and y-directions) with a standard deviation of 1.83 % (in contrast to 1.24 % and 1.01 % in the x- and y-directions, respectively). Along the z-direction (Fig. 9c), the porosity in the domain below slice #250 is ~15 %, and that in the domain above slice #250 is ~18 %. There are cyclic porosity fluctuations with a period of ~150 μm (60 pixels) associated with the size of a grain in each domain. The variogram in the z-direction (Fig. 9f) shows a larger variability than those in the other two directions, which refers to zonal anisotropy caused by layering (Gringarten and Deutsch, 2001). The spatial correlation range of ~875 μm (350 pixels) in the z-direction is associated with millimetre-scale layering, in contrast to the range of ~150 μm (60 pixels) in the x- and y-directions (Fig. 9 d, e) associated with the size of a grain.

To investigate the nature of the variability in the z-direction, a larger sub-sample (7145 x 7145 x 9330 μm^3) of sandstone S1 was imaged with a resolution of 5 μm (Fig. 10). A slice-by-slice porosity evaluation in the z-direction (Fig. 10c) shows two cycles with a period of ~3000 μm and a range of ~2000 μm (Fig. 10f). This is in addition to the finer-scale periodicity at ~150 μm, which was also observed in the x- and y-directions (Fig. 10d, e). Therefore, to capture this layering, a cube with an edge length of at least ~2000 μm, which was derived from the directional analysis, should be defined as the REV for S1. Alternatively, the REV from the classic approach was with an edge length of 475 voxels (~1187 μm, Appendix B, Figs. B1a, b). As the directional REV approach better captures the anisotropy in the sample structure, the entire specimen cube with an edge length of 2950 μm (~1.5 larger than the evaluated directional REV) scanned with a 2.5 μm resolution was chosen for the flow modelling.

https://doi.org/10.5194/se-2020-47
Preprint. Discussion started: 4 May 2020

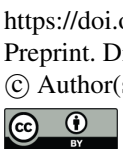

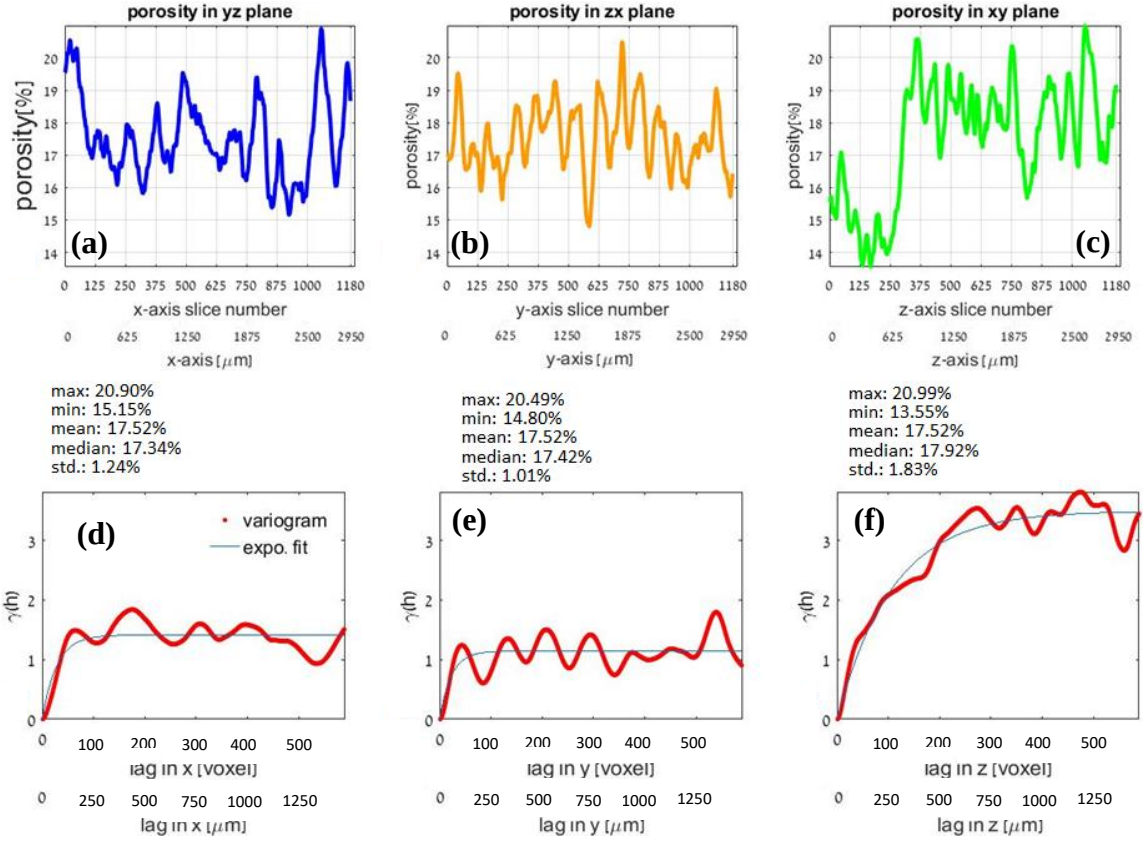

Figure 9: *Directional REV analysis of sandstone S1 scanned with a resolution of 2.5 μm. In the top row, the porosities calculated slice by slice for the x-, y- and z-directions are presented* ***(a-c)****. In the bottom row* ***(d-f),*** *the results of the variogram analysis are presented. The cyclicity in the variogram refers to the cyclicity of the porosity at the pore scale.*

https://doi.org/10.5194/se-2020-47
Preprint. Discussion started: 4 May 2020

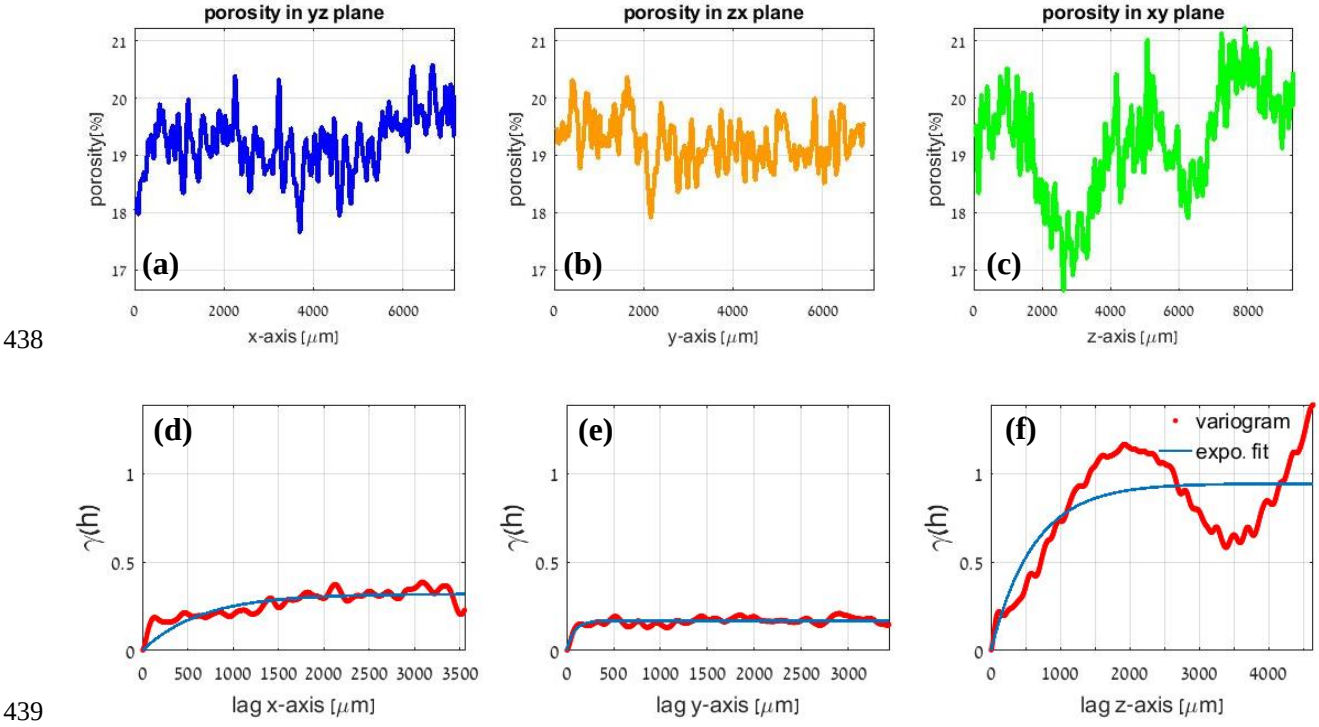

Figure 10: *Directional REV analysis for sandstone S1 scanned with a resolution of 5 μm. In the top row, the porosities calculated slice by slice for the x-, y- and z-directions are presented* ***(a-c)****. In the bottom row* ***(d-e)****, the variogram analysis shows cyclicity in the x- and y-directions associated with pore size fluctuations.* ***(f)*** *In the z-direction, the range of ~2000 μm is associated with porosity fluctuations between the high- and low-porosity bands separated by this distance.*

Figure 11 shows the results of the directional REV analysis for sample S2 conducted on a cube with an edge length of 2950 μm (1180 pixels) scanned with a 2.5 μm resolution. Each direction shows a remarkably different trend (Fig. 11a-c). The largest difference between the minimum and maximum slice porosities, 6.57 %, appears in the z- direction (in contrast to 4.5 % and 3.56 % in the x- and y-directions, respectively), and the standard deviation in the z-direction (1.53 %) is approximately twice those in the other two directions (0.86 % and 0.73 %). An increase in porosity with the slice number is observed in the z-direction (Fig. 11c) and is also represented by the trend in the variogram (Fig. 11f). This trend is inversely correlated with the content of clay between the sand grains (Fig. 11a-c, brown curve). The negative correlation coefficient between the porosity and clay matrix in the z-direction (-0.87) (Fig. 11g-i) is larger

https://doi.org/10.5194/se-2020-47
Preprint. Discussion started: 4 May 2020

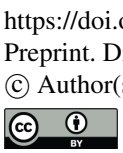

454 (in its absolute value) than the corresponding correlation coefficients in the x- and y-directions (-0.34 and -
455 0.03, respectively). Finally, the sill in the directional variogram analysis is not reached for S2 in the y- and
456 z-directions for the cube with an edge length of 2950 µm. Alternatively, the large difference between the
457 mean and median porosities from the classic REV approach (Appendix B, Fig. B1c, d) implies that the REV
458 also cannot be reached. As a result, flow modelling could not be conducted for sample S2.

459

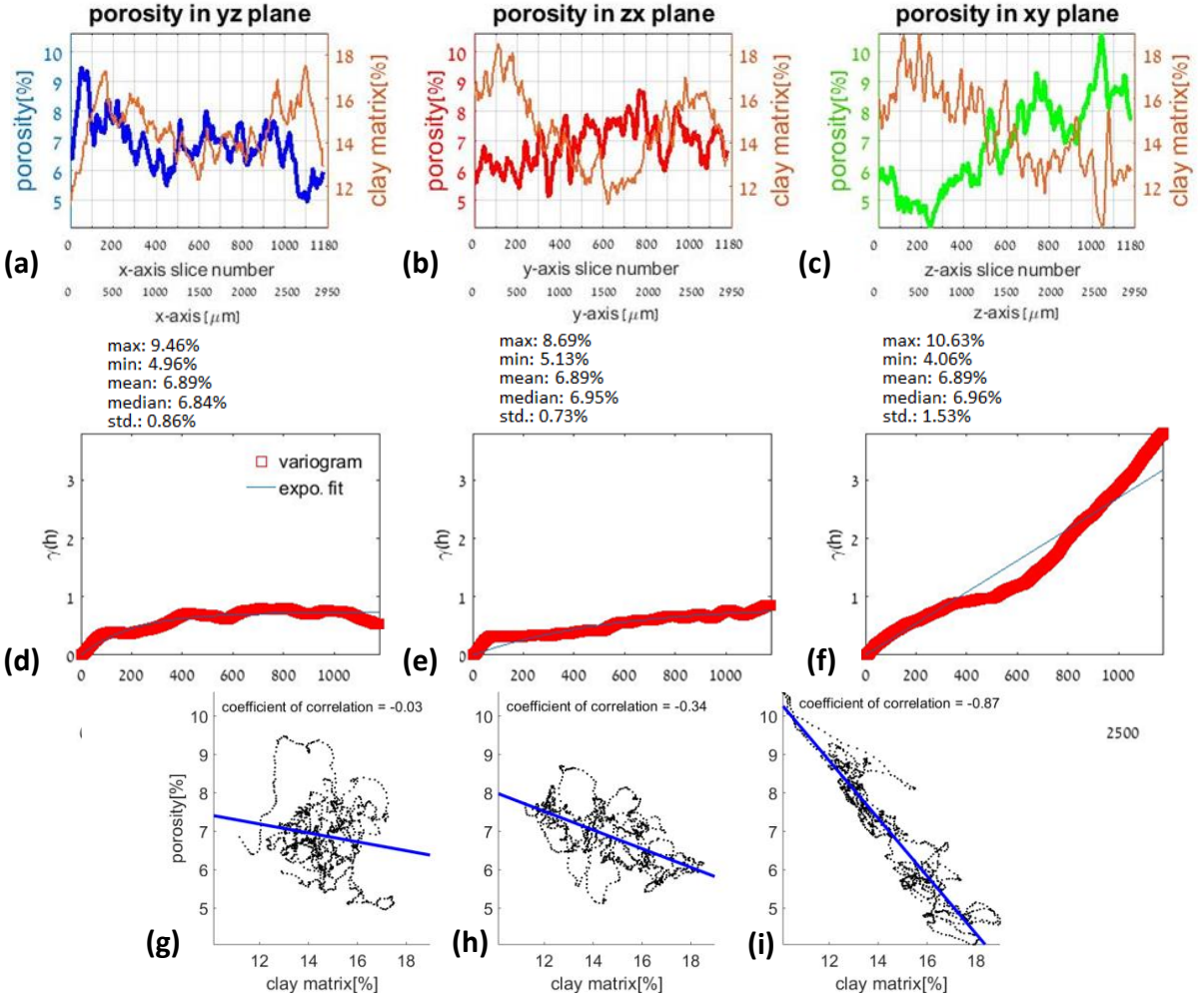

460

461 ***Figure 11:*** *Directional REV analysis for sandstone S2. In the top row, the porosities calculated slice by slice*
462 *for the x-, y- and z-directions and the fractions of the clay matrix are presented* ***(a-c)****. In the middle row* ***(d-f)****,*

https://doi.org/10.5194/se-2020-47
Preprint. Discussion started: 4 May 2020

*variogram analyses indicate that the sill is not reached for the y- and z-directions. Scatterplots **(g-i)** show the correlation of the porosity with the clay content, revealing a prominent inverse trend in the z-direction.*

Directional REV analysis conducted on the cube of sample S3 with an edge length of 2950 µm (1180 pixels) scanned with a 2.5 µm resolution indicates that all three directions show similar fluctuations around the mean porosity (Fig. 12a-c). The differences between the minimal and maximal IPs are 5.89 % in the y-direction and 5.45 % in the x- and z-directions. The standard deviation is similar in all directions. Variogram analysis (Fig. 12d-f) indicates similar sills (1.1-1.3) and ranges (~150 µm (60 pixels)) in all directions, indicating an isotropic pore network. Classic REV analysis (Appendix B, Fig. B1) yields an REV with a cube edge length of 875 µm (350 pixels), which is larger than the edge length of 150 µm from directional REV analysis. Therefore, the result of the classic REV analysis (875 µm or 350 pixels) was used in this study for the flow modelling.

https://doi.org/10.5194/se-2020-47
Preprint. Discussion started: 4 May 2020

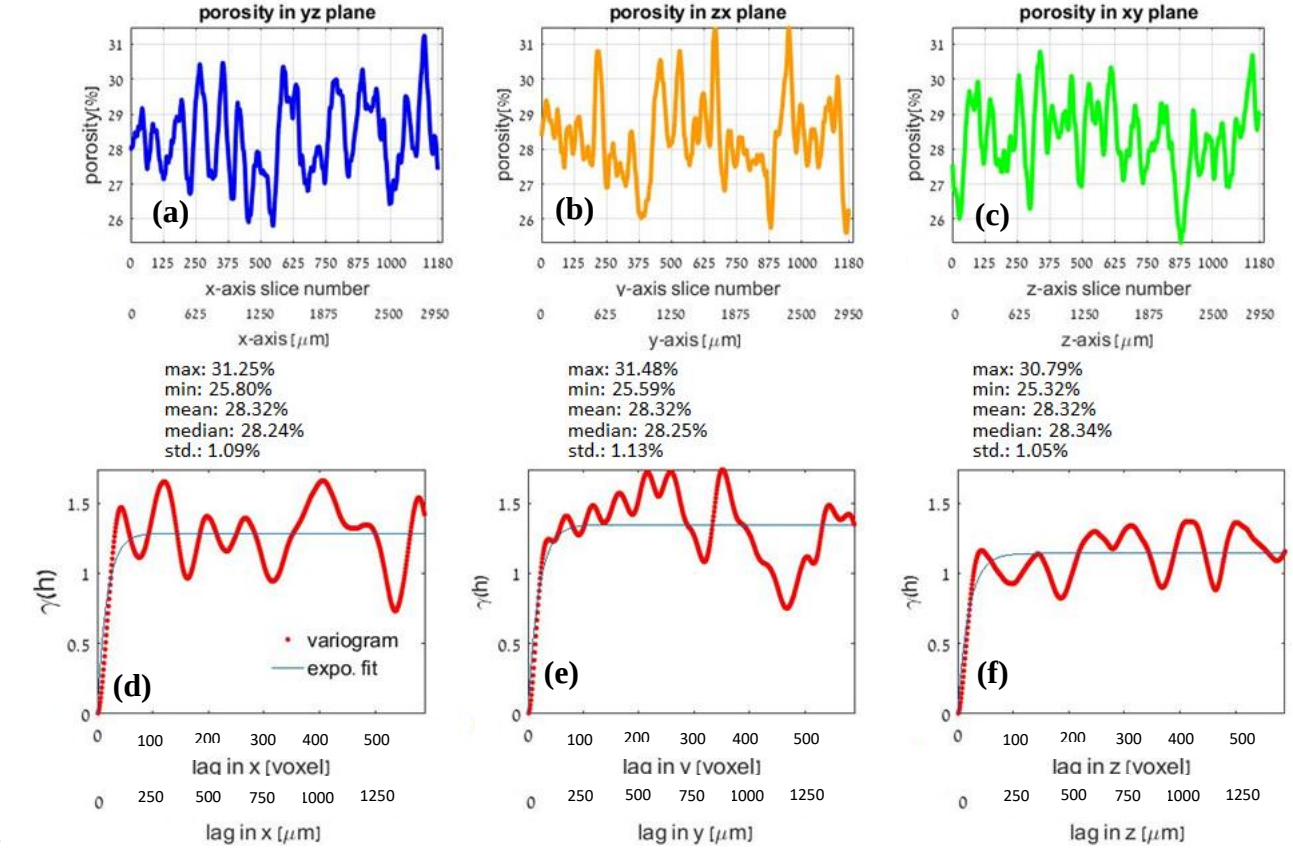

Figure 12: *Directional REV analysis for sandstone S3. In the top row, the porosities calculated slice by slice for the x-, y- and z-directions are presented* ***(a-c)****. In the bottom row* ***(d-f)****, the variogram analysis indicates the representativeness of the sample for relatively small sub-volumes with a cube edge length of ~150 μm (60 pixels).*

4.3. Fluid flow modelling at the pore scale

Fluid flow was modelled at the pore scale in two different micro-CT-scanned geometries: 1) a full cube of sample S1, including two adjacent parts possessing relatively low (0-250 voxels) and high (250-1180 voxels) porosities (Fig. 9c), and 2) sample S3 within its REV dimensions (Table 3). Modelling of the 3D geometry of sample S2 was not performed due to the reasons detailed above. A constant pressure gradient of 2.424 $\left[\frac{Pa}{mm}\right]$ between the inlet and outlet boundaries was applied in all the simulations for consistency.

https://doi.org/10.5194/se-2020-47
Preprint. Discussion started: 4 May 2020

Table 3. *Porosity losses in S1 and S3 over the course of applying the extended computational workflow (Fig. 2).*

Sample	Sample size (mean mesh edge size) [μm]	CT segmented image porosity (%)	Connected porosity (%)	Mesh porosity (%)	Gas porosity (%)
S1 (entire sample, 1180 voxels)	2950 (14)	17.5	15.6	13.6	28
S3 (REV, 350 voxels)	875 (5)	28.3	27.9	25.9	31

The porosity of the meshed domain of sample S1 is 13.6 % (in contrast to 17.5 % in the segmented image, Table 3), and the mesh edge length is 14 µm along the pore walls. The observed porosity loss results from disconnecting narrow pore throats from the connected cluster imaged with a 2.5 µm voxel size due to the use of a 14 µm mesh size (the lowest possible for our computational needs). A maximum Reynolds number of $Re = 0.084$ was used to guarantee the simulation in a creeping flow regime.

The symmetrized permeability tensor, $\bar{\bar{\kappa}}$, was obtained as follows (Table 2):

$$\bar{\bar{\kappa}}_{sym} = \begin{pmatrix} 420 & 66.3 & 1.91 \\ 66.3 & 344 & 12.8 \\ 1.91 & 12.8 & 163 \end{pmatrix}$$

The permeability tensor is anisotropic, with κ_{zz} being more than half κ_{xx} and κ_{yy}. This result is in agreement with the appearance of horizontal banding with higher cementation derived from the variogram analysis (Fig. 10f).

The porosity of the meshed domain of sample S3 is 25.9 % (in contrast to 28.3 % in the segmented image, Table 3), and the mesh edge length is 5 µm along the pore walls. A maximum Reynolds number of $Re = 0.22$ was used to guarantee the simulation in a creeping flow regime. The symmetrized permeability tensor is close to isotropic (Table 2):

$$\bar{\bar{\kappa}}_{sym} = \begin{pmatrix} 4517 & 5 & 38 \\ 5 & 4808 & 547 \\ 38 & 547 & 4085 \end{pmatrix}$$

https://doi.org/10.5194/se-2020-47
Preprint. Discussion started: 4 May 2020


Solid Earth Discussions

505 The tortuosity of S3 in the x-, y-, and z- directions varies in the range [1.39, 1.47] (Table 2), and the
506 largest value is observed in the z-direction, which is in agreement with the lowest permeability in the z-
507 direction.

508 **4.4. Image analysis**

509 For S1, the mode peak of the pore size distribution (measured by a Feret maximum calliper) (Fig. 13,
510 red line) is at 194 μm (Table 2). In total, 3500 pores were analysed. The pore specific surface area (*PSA*)
511 calculated from micro-CT images is $0.068\ \mu m^{-1}$. The tortuosity, measured from the whole CT image,
512 indicates similar values in the x- and y-directions of 1.37 and 1.38, respectively, whereas in the z-direction,
513 the tortuosity is 1.48 (Table 2). As many paths were considered, we suggest that this difference is created by
514 the textural features that appear in horizontal planes (Fig. 3a).

515 For S2, the mode peak of the pore size distribution (Fig. 13, blue line) is at 21 μm. A large pore
516 population is also recognized at ~100 μm (Table 2). In total, 45000 pores were analysed. The pore specific
517 surface area (*PSA*) calculated from micro-CT images is
518 $0.136\ \mu m^{-1}$ (Table 2), which is twice as large as the *PSA* of S1.

519 For S3, the pore size distribution (Fig. 13, green line) has a mode peak at 223 μm and shows a
520 Gaussian shape (Table 2). In total, 3491 pores were analysed. The geometry-based tortuosity values
521 measured from the whole CT image with multiple paths is 1.32, 1.34 and 1.39 in the x-, y- and z-directions,
522 respectively. The tortuosity is lower for S3 than for S1 in all directions, which is a direct result of the smaller
523 amount of cement in the pore throats. The *PSA* of S3 is $0.069\ \mu m^{-1}$, which is similar to that of S1.

https://doi.org/10.5194/se-2020-47
Preprint. Discussion started: 4 May 2020

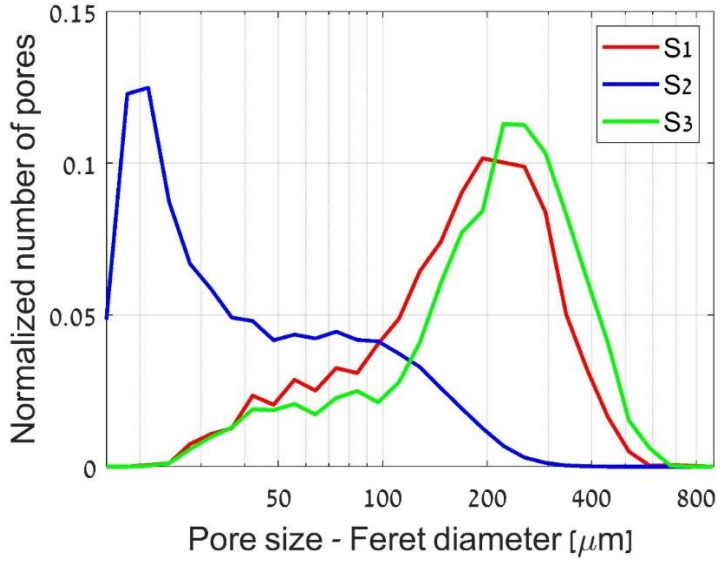

Figure 13: *Statistics of the pore sizes calculated by image analysis for three sandstone samples: S1, S2, and S3.*

5. Discussion

5.1. Validation of permeability by micro- and macro-scale rock descriptors

Each of the evaluated micro- and macro-scale rock descriptors supplies qualitative information about the sample permeability (Tables 2-3), which is used to validate the multi-methodological approach presented in this paper. Specifically, the increasing mercury effective saturation with increasing pressure shows a similar *PTSD* curve slope for sandstone samples S1 and S3 in the macro-pore throat range (Fig. 7), suggesting that these samples have similar structural connectivity. However, S1 has a smaller volume fraction of pore space available for fluid flow that is controlled by macro pore throats (i.e., 81 % in S1 vs. 93 % in S3, Fig. 7) due to its higher contents of silt, clay, and Fe-ox cement. The intermediate layer (S2) comprises more fines, which form a clay matrix with 19 % porosity, most likely affected by the burial conditions of this sample (Table 2). Only ~15 % of the pore volume fraction in S2 is controlled by bottle-neck macro pore throats (Fig. 7). However, the characteristic length of S2, 12.3 µm (Table 2), indicates that

https://doi.org/10.5194/se-2020-47
Preprint. Discussion started: 4 May 2020

macro-pore connectivity is still possible even when the pore space consists mainly of sub-macro-scale porosity. This 0.15 volume fraction is in agreement with Harter (2005), who estimated a volume fraction threshold of 0.13 for correlated yet random 3D fields required for full interconnectivity.

The value of the connectivity index of S3 (10) is approximately three times higher than that of S1 (3.49), while both rocks are defined as moderately sorted sandstones (Table 2). This difference is due to S1 having a smaller number of inequivalent loops within the pore network than S3 (Appendix C), leading to smaller β_1 values in Euler characteristics. Inequivalent loops are correlated with pore throats; their number is affected by the resolution of the CT image and by the partial volume effect at grain surfaces (Cnudde and Boone, 2013; Kerckhofs et al., 2008), where some voxels could be identified as grains and thus "clog" the small pore throats. Artefact porosity loss is apparent for S1, where the IP is 17.5 % (in contrast to the CT porosity of 23.5 % predicted from MIP, Table 2). The connectivity index of S2 (0.94, Table 2) is lower than those of both S1 and S3 because of the clay matrix, which clogs pores. The effect of the partial volume effect on the image connectivity and on the preservation of small features was reviewed by Schlüter et al. (2014).

A correlation was found between the grain size and the amount of Fe-ox cement in S1 evaluated at each slice along the z-direction (from the image analysis, Fig. 14). Exceptionally large grains are detected (indicated by the red rectangle) near the cemented region at ~750 μm. Large grains and a relatively high amount of cement can also be observed in the S1 thin section (Fig. 3b). Large grains cause large pores and generate relatively permeable horizons through which water flow and solute transport can become focused (McKay et al., 1995; Clavaud et al., 2008), supplying iron solutes. We suggest that a vadose zone was formed after flooding events, where the water flow mechanism could have changed from gravity dominated to capillary dominated. Water then flowed due to capillary forces along grain surfaces towards regions with larger surface areas, and iron solutes precipitated in a reaction with oxygen available in the partly saturated zone. We suggest that with time, this cementation mechanism caused a decrease in the pore throat size near the preferential path, while the preferential path with a low surface area remained open, eventually generating the observed anisotropic flow pattern.

https://doi.org/10.5194/se-2020-47
Preprint. Discussion started: 4 May 2020

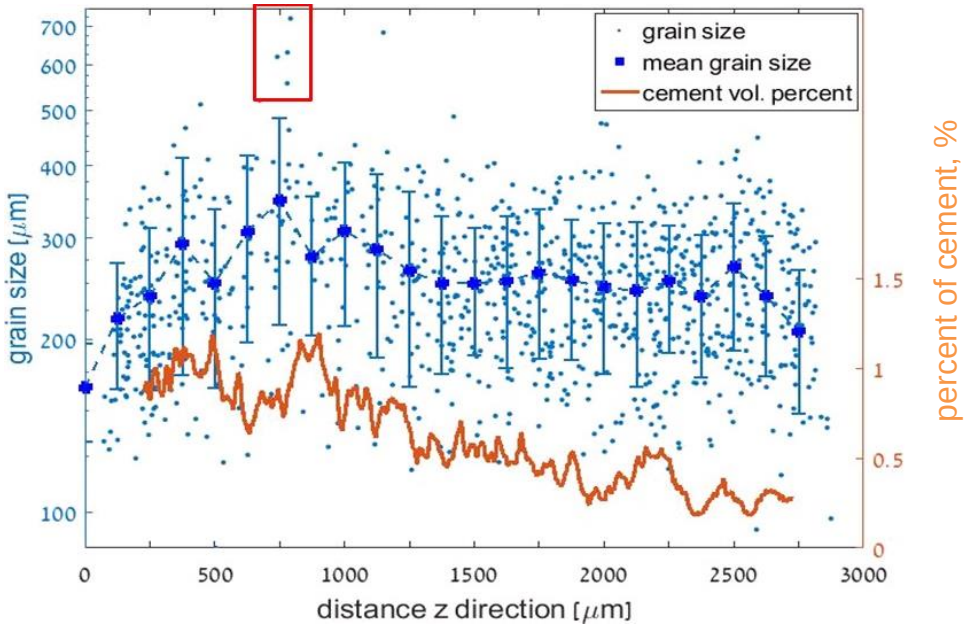

Figure 14. *Grain size scattering and Fe-ox cement content in sandstone S1 in slices along the z-direction.*

In this respect, permeability anisotropy in sandstones at a small scale is usually attributed to the shape or preferential orientation of grains and pores (e.g., Sato et al., 2019) and to a heterogeneous distribution of cementing material at grain contacts (Louis et al., 2005). At a larger scale, a higher degree of permeability anisotropy is associated with the presence of localized beds, foliation, and compaction bands that constitute barriers to flow in the perpendicular direction (see Halisch et al., 2009; Clavaud et al., 2018 and references therein). Clay-free and cement-free layers constitute the main avenues for flow in the parallel direction (e.g., Fig. 14).

The directional REV analysis of S1 reveals porosity bands with a period of 2 mm perpendicular to the z-direction (Fig. 10c, f) that are composed of sub-domains exhibiting high and low Fe-ox cementation. Flow modelling in the specified REV shows anisotropy (Table 2) and an average permeability value of 310 mD that is close to that derived from MIP (330 mD). However, the average permeability is lower than the average experimental gas permeability (~543 mD); this difference should be related to the loss of porosity due to limitations on the CT resolution, image processing and meshing (Table 3, see Sect. 5.2 for more details).

https://doi.org/10.5194/se-2020-47
Preprint. Discussion started: 4 May 2020

582 In contrast, no banding was detected in S3 by the directional REV analysis (Fig. 12). Flow modelling
583 and upscaling to the macro scale indicate an isotropic sample (Table 2), which agrees with the isotropy
584 derived from the variogram analysis. However, the modelled permeability (~4500 mD) is ten times higher
585 than the MIP-derived permeability (466 mD, Table 2). Gas permeability measurements indicate anisotropy,
586 yielding permeabilities of 4600 mD in the x-y plane and 220 mD in the z-direction (with an anisotropy ratio
587 of ~20, defined here as $\kappa_{\parallel}/\ \kappa_{\perp}$, e.g., Tiab and Donaldson, 2004). For comparison, the values of this ratio
588 obtained from experimental permeability measurements were ~1.2 for Bentheim sandstone (Louis et al.,
589 2005), ~1.7-2.5 for a sandstone within the Cretaceous Virgelle Member, Alberta, Canada (Meyer and
590 Krause, 2001), and ~8.5 for Berea sandstone (Sato et al., 2019). However, in some laboratory measurements
591 conducted parallel to the layering (in the x-y plane), poorly cemented grains in S3 were dislocated from the
592 weakly consolidated sample due to the application of a pressure gradient. This could have resulted in a
593 higher measured gas flux and thus a higher permeability parallel to the layering, yielding a high anisotropy.
594 In this case, the permeability upscaled from the modelling in S3 is also exaggerated.

595 Alternatively, the disagreement between the laboratory-determined permeability (perpendicular to the
596 layering) and the permeability obtained from the flow modelling (Table 2) may also stem from the small
597 dimension of the modelled domain (cube edge length of ~0.875 mm), which may not have included the
598 textural features that constrain fluid flow on a larger scale (e.g., Fig. 5d).

599 For sample S2, both REV analyses indicated an REV size much larger than the investigated sample
600 size (Fig. 11, Figs. B1 c,d in Appendix B). For this reason, the analytical programme formulated in our
601 paper cannot entirely be applied to S2 due to the impossibility of determining a reliable REV and hence
602 conducting pore-scale flow modelling. As a result, although sample S2 represents a common sandstone, it is
603 of a very heterogeneous nature, and a sample larger than 3 mm is required to capture its REV. The MIP-
604 derived permeability is 4 mD; this low permeability is due to a clay-rich matrix that encloses substantial
605 void space (Hurst and Nadeau, 1995; Neuzil, 2019). The gas permeability of the quartz wacke layer (S2,
606 ~4.6 mD on average) is approximately 2 orders of magnitude lower than that of the quartz arenite layers (S1
607 and S3, Table 2). The permeability anisotropy ratio in S2 is ~2.8. The high inverse correlation between the
608 porosity and clay matrix content enhanced in the z-direction (Fig. 11 g-i) suggests that the clay matrix
609 pattern appears as horizontal layering, thus generating the observed anisotropy.

https://doi.org/10.5194/se-2020-47
Preprint. Discussion started: 4 May 2020

610

611 **5.2. Upscaling permeability: accuracy of the extended computational workflow**

612 The extended computational workflow (Fig. 2) serves as the main tool in this study for upscaling
613 permeability from the pore-scale velocity field. The accuracy of each step in the workflow affects the
614 ultimate result.

615 Following the steps of the workflow (Fig. 2), a micro-CT image resolution of 2.5 μm limits the
616 reliability of the representation of the porous medium and defines the lower pore identification limit using
617 this method. As an example of this limitation, the *SSA* (bulk specific surface area) calculated by MIP is
618 larger than the *PSA* (pore specific surface area) calculated by micro-CT image analysis in all the samples
619 (Table 2), although the pore volume is always smaller than the bulk volume. The *PSA* from micro-CT is
620 limited by the image resolution and therefore does not consider relatively small pores with large surfaces.
621 The *PSA*s of S1 and S3 are similar, but the *SSA* (from MIP) of S1 is 20 times larger than that of S3 because
622 S1 has a larger surface area at small pores created mainly by Fe-ox cement (compare Fig. 3c-f for S1 to Fig.
623 5c for S3). S2 shows a *PSA* twice as large as that of S1 due to the presence of clay and clay matrix with
624 large surface areas.

625 Image processing and segmentation were applied in this study to recover the image geometry, which
626 was blurred by noise or affected by the partial volume effect (see Sect. 3). Then, the loss of pore space due
627 to the resolution limits was estimated in this study from the amount of mercury filling the pores with
628 diameters equal to the resolution limit (Fig. 7a). After segmentation, sample S1 had a segmented image
629 porosity of 17.5 % and a CT predicted porosity of 23.5 % from MIP (Tables 2, 3). Therefore, the difference
630 in porosities generated by the partial volume effect in the image processing scheme (e.g., Cnudde and
631 Boone, 2013) is a significant component of error, especially for small structures, such as pores with a large
632 surface area-to-volume ratio. In contrast, the image porosity of S3 after segmentation was 28.3 %, which is
633 close to the porosity of 30.4 % estimated from MIP (Tables 2, 3). This is a result of the very small degree of
634 cementation and the absence of Fe-ox flakes in the majority of the sample pores, leading to the small
635 contribution of the partial volume effect. In comparison, a fine-grained and well-sorted Lower Cretaceous
636 Fm. sandstone from Heletz Field (e.g., Fig. 1a) (Tatomir et al., 2016) comprising clay and calcite had MIP
637 and micro-CT porosities of 26.7 % and 20.9 %, respectively.

https://doi.org/10.5194/se-2020-47
Preprint. Discussion started: 4 May 2020

638 An additional source of inaccuracy is the use of a porosity-based REV for permeability
639 approximations. Mostaghimi et al. (2013) showed that for CT images of sandpacks (homogenous samples),
640 the porosity-based REV had an edge length of 0.5 mm, whereas the permeability-based REV was twice as
641 large. Moreover, the porosity- and permeability-based REVs in images of bead packs derived by Zhang et
642 al. (2000) had edge lengths of 1.71 and 2.57 mm, respectively. According to Mostaghimi et al. (2013), larger
643 REV values for permeability rely on contributions from the tortuosity and connectivity of pore spaces,
644 whereas the larger REV values of Zhang et al. (2000) may be related to the heterogeneity of the sample.

645 Further, textural bedding at a 2 mm scale dominates the porosity anisotropy in S1 (Fig. 10f, evaluated
646 by the directional REV, e.g., Halisch, 2013). To upscale to permeability reliably, the REV domain should be
647 sufficiently large such that it is bounded from below by the scale of the textural bedding (i.e., an edge length
648 > 2 mm) but should not be larger than necessary to optimize computational efficiency (while remaining
649 within the same scale of heterogeneity, i.e., at the macro scale). As a result, a REV consisting of an edge
650 length of ~2950 μm (~1.5 times larger than the scale of textural bedding) was chosen in the current study in
651 sample S1. For comparison, in other studies, the edge lengths of REVs in sandstones were 0.68 mm (Ovaysi
652 and Piri, 2010), 0.8 mm (Mostaghimi et al., 2013), and 1.2 mm (Okabe and Oseto, 2006; Tatomir et al.,
653 2016). The larger REV size in the current study found by the directional approach (rather than by the classic
654 isotropic approach) was due to the textural features revealed in the z-direction.

655 Another source of inaccuracy is the geometry used for the flow model. The geometry considered in
656 this study included only the pore network connecting six faces of the REV cube. Other pore spaces in the
657 REV disconnected from the main network were deleted (because all paths smaller than the resolution were
658 prescribed as grain pixels due to the partial volume effect), thus resulting in the smaller effective size of the
659 simulation domain. The image porosity of sample S1 was 17.5 %, whereas its connected porosity was
660 estimated as 15.6 % (Table 3), while those of sample S3 were 28.3 % and 27.9 %, respectively.

661 Furthermore, the mesh was generated by taking a trade-off between the size of the mesh elements (4
662 elements in the smallest pore throat) and computational limits into account while coarsening the mesh
663 elements towards the pore centre. The connectivity between pores with very fine pore throats that could not
664 be replaced by mesh elements could be lost, resulting in the loss of those pores in the calculations. In sample
665 S1, the porosity used in the simulation was approximately 50 % smaller than the porosity estimated by gas

https://doi.org/10.5194/se-2020-47
Preprint. Discussion started: 4 May 2020

porosimetry (Tables 2, 3). In contrast, the porosity used to simulate S3 was mostly preserved, comprising ~84 % of that estimated in the laboratory.

For comparison, in the fine-grained sample of the Lower Cretaceous sandstone from Heletz Field in Israel (Fig. 1a), which has grain size characteristics similar to those of S1 but with higher clay and additional calcite contents (Tatomir et al., 2016), the permeability upscaled from micro-CT flow modelling (conducted by the same simulation method as that in the current study) exceeded the gas permeability by a factor of ~6. This could be related either to the small REV for the flow model or to the reduction in the specific surface area by image processing and meshing (Mostaghimi et al., 2013) for the flow modelling.

Finally, the upscaling process from the flow modelling successfully predicted the permeability anisotropy ratio of ~ 2.3 in S1, as discussed above. For comparison, the permeability anisotropy ratio evaluated using micro-CT flow monitoring in clay-free sandstones (Clavaud et al., 2008) had a mean value of ~2.5 (ranging from ~1.7 to ~5.2), related to the presence of less permeable silty layers. This is consistent with the ratio estimated at the pore scale in Rothbach sandstone (~5) (Louis et al., 2005), attributed to lamination due to differences both in the characteristics of the solid phase (grain size and packing) and in the content of Fe oxides.

6. Conclusions

This paper presents a detailed description and evaluation of a multi-methodological petrophysical approach for the comprehensive multiscale characterization of reservoir sandstones. The validation was performed on samples from three different consecutive layers of Lower Cretaceous sandstone in northern Israel. The following conclusions can be drawn:

1. The suggested methodology enables the identification of links between Darcy-scale permeability and an extensive set of geometrical, textural and topological rock descriptors, which are quantified at the pore scale by deterministic and statistical methods. Specifically, micro-scale geometrical rock descriptors (grain and pore size distributions, pore throat size, characteristic length, pore throat length of maximal conductance, specific surface area, and

https://doi.org/10.5194/se-2020-47
Preprint. Discussion started: 4 May 2020

connectivity index) and macro-scale petrophysical properties (porosity and tortuosity), along with quantified anisotropy, are used to predict the permeability of the studied layers.

2. Laboratory porosity and permeability measurements conducted on centimetre-scale samples show less variability for the quartz arenite (top and bottom) layers and more variability for the quartz wacke (intermediate) layer. The magnitudes of this variability in the samples are correlated with the dimensions of their representative volumes and anisotropy, both of which are evaluated within the micro-CT-imaged 3D pore geometry. This variability is associated with clay and cementation patterns in the layers and is quantified in this study with image analysis.
3. Two different scales of porosity variations are revealed in the top layer by statistical variogram analysis: fluctuations at 150 μm are due to variability in grain and pore sizes, and those at 2 mm are due to the occurrence of high- and low-porosity bands occluded by Fe-ox cementation. The latter millimetre-scale variability is found to control the macroscopic rock permeability measured in the laboratory. Bands of lower porosity could be generated by Fe-ox cementation in regions with higher surface areas adjacent to preferential fluid flow paths.
4. The macroscopic permeability upscaled from the pore-scale velocity field simulated by flow modelling in the micro-CT-scanned geometry of millimetre-scale sample shows agreement with laboratory petrophysical estimates obtained for centimetre-scale samples for the quartz arenite (top) layer. The anisotropy in both estimates correlates with the presence of millimetre-scale bedding, also recognized by the variogram analysis.
5. The multi-methodological petrophysical approach detailed and evaluated in this paper is particularly applicable for the detection of anisotropy at various rock scales and for the identification of its origin. Moreover, this method allows the accurate petrophysical characterization of reservoir sandstones with broad ranges of textural and topological features.

Acknowledgements

This project was supported by fellowships from the Ministry of Energy, Israel, and the University of Haifa. The authors are grateful to Igor Bogdanov from the University of Pau for his continuing scientific support. Special thanks to Rudy Swennen and his group from KU Leuven for their contributions to the MIP,

https://doi.org/10.5194/se-2020-47
Preprint. Discussion started: 4 May 2020

721 thin section preparation, microscopy and micro-CT image processing; to Veerle Cnudde and her group from
722 Ghent University for teaching us the image processing techniques; to Kirill Gerke and Timofey Sizonenko
723 from the Russian Academy of Sciences for providing their image processing code; to Uzi Saltzman from
724 Engineering Geology and Rock Mechanics Company, Israel, for sending his detailed historic geological
725 description of the study area; and to Or Bialik, Nimer Taha and Ovie Emmanuel Eruteya from the
726 University of Haifa, Israel, for their assistance in the laboratory work.
727

728 **Competing interests**

729 The authors declare that they have no conflicts of interest.
730

731 **Author contributions.** PH and RK designed the study. PH developed codes for pore-scale modelling with
732 contributions by RK and MH. BS advised the microscopy and led the geological interpretations. MH scanned
733 the samples and contributed to the statistical analysis conducted by PH. NW led the laboratory
734 measurements. All co-authors participated in the analysis of the results. PH wrote the text with contributions
735 from all co-authors. All co-authors contributed to the discussion and approved the paper.
736

https://doi.org/10.5194/se-2020-47
Preprint. Discussion started: 4 May 2020

References

Abed, A. M.: Depositional environments of the early cretaceous Kurnub (Hatira) sandstones, North Jordan, Sedimentary Geology, 31(3-4), 267-279, **1982**.

Adams, A. E., MacKenzie, W. S., and Guilford, C.: Atlas of sedimentary rocks under the microscope. Routledge, Taylor and Francis Group, London and New York, **2017**.

Akinlotan, O.: Porosity and permeability of the English (Lower Cretaceous) sandstones, Proceedings of the Geologists' Association, 127(6), 681-690., **2016**.

Akinlotan, O.: Mineralogy and palaeoenvironments: the Weald Basin (Early Cretaceous), Southeast England, The Depositional Record, 3(2), 187-200, **2017**.

Amireh, B. S.: Sedimentology and palaeogeography of the regressive-transgressive Kurnub Group (Early Cretaceous) of Jordan, Sedimentary Geology, 112(1-2), 69-88., **1997**.

Andrä, H., Combaret, N., Dvorkin, J., Glatt, E., Han, J., Kabel, M., Keehm. Y., Krzikalla, F., Lee, M., Madonna, C., Marsh, M., Mukerji, T., Saenger, E., Sain, R., Saxena, N., Ricker, S., Wiegmann, A., and Zhan, X.: Digital rock physics benchmarks-Part II: Computing effective properties, Computers & Geosciences, 50, 33-43, **2013**.

Avigad, D., Kolodner, K., McWilliams, M., Persing, H., and Weissbrod, T.: Origin of northern Gondwana Cambrian sandstone revealed by detrital zircon SHRIMP dating, Geology, 31(3), 227-230, **2003**.

Avigad, D., Sandler, A., Kolodner, K., Stern, R. J., McWilliams, M., Miller, N., and Beyth, M.: Mass-production of Cambro-Ordovician quartz-rich sandstone as a consequence of chemical weathering of Pan-African terranes: Environmental implications, Earth and Planetary Science Letters, 240(3-4), 818-826, **2005**.

Bachmann, M., and Hirsch, F.: Lower Cretaceous carbonate platform of the eastern Levant (Galilee and the Golan Heights): stratigraphy and second-order sea-level change, Cretaceous Research, 27(4), 487-512, **2006**.

Bear, J., Dynamics of Fluids in Porous Media. Courier Corporation, **1988**.

Blunt, M. J., Bijeljic, B., Dong, H., Gharbi, O., Iglauer, S., Mostaghimi, P., Paluszny, A., and Pentland, C.: Pore-scale imaging and modelling, Advances in Water Resources, 51, 197-216, **2013**.

Boek, E. S., and Venturoli, M.: Lattice-Boltzmann studies of fluid flow in porous media with realistic rock geometries, Computers & Mathematics with Applications, 59(7), 2305-2314, **2010**.

Bogdanov, I. I., Guerton, F., Kpahou, J., and Kamp, A. M.: Direct pore-scale modeling of two-phase flow through natural media, in: Proceedings of the 2011 COMSOL Conference in Stuttgart, **2011**.

Bogdanov, I. I., Kpahou, J., and Guerton, F.: Pore-scale single and two-phase transport in real porous medium, in: Proceedings of ECMOR XIII-13th European Conference on the Mathematics of Oil Recovery, September, **2012**.

Borgomano, J., Masse, J. P., Fenerci-Masse, M., and Fournier, F.: Petrophysics of Lower Cretaceous platform carbonate outcrops in Provence (SE France): implications for carbonate reservoir characterisation, Journal of Petroleum Geology, 36(1), 5-41, **2013**.

https://doi.org/10.5194/se-2020-47
Preprint. Discussion started: 4 May 2020

774 Boudreau, B. P.: The diffusive tortuosity of fine-grained unlithified sediments, Geochimica et Cosmochimica
775 Acta, 60(16), 3139-3142, **1996**.
776 Brabant, L., Vlassenbroeck, J., De Witte, Y., Cnudde, V., Boone, M. N., Dewanckele, J., and Van
777 Hoorebeke, L.: Three-dimensional analysis of high-resolution X-ray computed tomography data with
778 Morpho+, Microscopy and Microanalysis, 17(2), 252-263, **2011**.
779 Brunke, O., Brockdorf, K., Drews, S., Müller, B., Donath, T., Herzen, J., and Beckmann, F.: Comparison
780 between X-ray tube based and synchrotron radiation based μCT, in: Developments in X-ray
781 Tomography VI, edited by: Stock, S. R., San Diego: SPIE, 7078, **2008**.
782 Calvo, R., Ayalon, A., Bein, A., and Sass, E.: The diagenesis history of Heletz formation and the timing of
783 hydrocarbon accumulation in Heletz-Kokhav oil field, Geological Survey of Israel, Current Research, 8,
784 82-83, **1993**.
785 Calvo, R., Ayalon, A., Bein, A., and Sass, E.: Chemical and isotopic composition of diagenetic carbonate
786 cements and its relation to hydrocarbon accumulation in the Heletz-Kokhav oil field (Israel), Journal of
787 Geochemical Exploration, 108(1), 88-98, **2011**.
788 Carman, P. C.: Fluid flow through granular beds, Trans. Inst. Chem. Eng., 15, 150-166, **1937**.
789 Cerepi, A., Durand, C., and Brosse, E.: Pore microgeometry analysis in low-resistivity sandstone reservoirs,
790 Journal of Petroleum Science and Engineering, 35(3-4), 205-232, **2002**.
791 Clavaud, J. B., Maineult, A., Zamora, M., Rasolofosaon, P., and Schlitter, C.: Permeability anisotropy and its
792 relations with porous medium structure, Journal of Geophysical Research: Solid Earth, 113(B1), **2008**.
793 Cnudde, V., and Boone, M. N.: High-resolution X-ray computed tomography in geosciences: A review of the
794 current technology and applications, Earth-Science Reviews, 123, 1-17, **2013**.
795 Cohen, A., and Boehm, S.: Lithofacies and environments of deposition of the Lower Cretaceous Helez &
796 Telamim Formations, Geological Survey of Israel Report No. 5, **1983**.
797 Cohen, Z.: The geology of the Lower Cretaceous in Southern Coastal Plain, Ph.D. thesis, The Hebrew
798 University of Jerusalem, 98 pp. (in Hebrew, with English abstract), **1971**.
799 Cressie, N.: Statistics for spatial data, Terra Nova, 4(5), 613-617, **1992**.
800 Djebbar, T., and Donaldson, E. C.: Petrophysics. Elsevier Engineering Information Incorporated, **2004**.
801 Dullien, F. A.: Porous media: fluid transport and pore structure, Academic press, **2012**.
802 Harter, T.: Finite-size scaling analysis of percolation in three-dimensional correlated binary Markov chain
803 random fields, Physical Review E, 72(2), 026120, **2015**.
804 Ferreira, N. N., Ferreira, E. P., Ramos, R. R., and Carvalho, I. S.: Palynological and sedimentary analysis of
805 the Igarapé Ipiranga and Querru 1 outcrops of the Itapecuru Formation (Lower Cretaceous, Parnaíba
806 Basin), Brazil, Journal of South American Earth Sciences, 66, 15-31, **2016**.
807 Folk, R. L., and Ward, W. C.: Brazos River bar [Texas]; a study in the significance of grain size parameters,
808 Journal of Sedimentary Research, 27(1), 3-26, **1957**.
809 Foos, A. M., Regional hydrogeology of the Sharon Aquifer, in: Pennsylvanian sharon formation, past and
810 present: sedimentology, hydrology, historical and environmental significance, edited by: Foos, A. M.,

https://doi.org/10.5194/se-2020-47
Preprint. Discussion started: 4 May 2020

Guidebook No. 18, Ohio Department of Natural Resources, Division of Geology, Columbus OH, Chapter 4, 19-25, **2003**.

Gardosh, M. A., and Tannenbaum, E.: The petroleum systems of Israel, in: Petroleum systems of the Tethyan region: AAPG Memoir, edited by: Marlow, L., Kendall, C., and Yose, L., 106, 179-216, **2014**.

Garfunkel, Z.: The pre-quaternary geology in Israel, in: The zoogeography of Israel, edited by: Tchernov, E., and Yom-Tov, Y., Dr W. Junk Publishers, Dordrecht, Netherlands, 7-34, **1988**.

Garfunkel, Z.: History and paleogeography during the Pan-African orogen to stable platform transition: reappraisal of the evidence from the Elat area and the northern Arabian-Nubian Shield, Israel Journal of Earth Sciences, 48, 135-157, **1999**.

Giesche, H.: Mercury porosimetry: a general (practical) overview. Particle & particle systems characterization, 23(1), 9-19, **2006**.

Grader, P., and Reiss, Z.: On the Lower Cretaceous of the Heletz area, Geological Survey of Israel, Bull No. 16, 14 pp., **1958**.

Grader, P.: The geology of the Heletz oil field, Ph.D. thesis, The Hebrew University of Jerusalem, 81 pp. (in Hebrew, with English abstract), **1959**.

Gringarten, E., and Deutsch, C.V.: Teacher's aide variogram interpretation and modeling. Mathematical Geology, 33(4), 507-534, **2001**.

Guibert, R., Horgue, P., Debenest, G., and Quintard, M.: A comparison of various methods for the numerical evaluation of porous media permeability tensors from pore-scale geometry, Mathematical Geosciences, 48(3), 329-347, **2016**.

Haldorsen, H. H., and Lake, L. W.: A new approach to shale management in field-scale models, Society of Petroleum Engineers Journal, 24(04), 447-457, **1984**.

Halisch, M.: Application and assessment of the lattice boltzmann method for fluid flow modeling in porous rocks, PhD thesis, Technical University of Berlin, 182 pp., **2013**.

Halisch, M.: The REV Challenge – estimating representative elementary volumes and porous rock inhomogeneity from high resolution micro-CT data sets, Society of Core Analysts (SCA) Proceedings, SCA2013-069, **2013**.

Halisch, M., Weller, A., Debschütz, W., Sattler, C. D., and El-Sayed, A. M.: A complex core-log case study of an anisotropic sandstone, originating from Bahariya Formation, Abu Gharadig Basin, Egypt, Petrophysics, 50(06), **2009**.

Haoguang, W. E. I., Kun, M. A., Xiang'an, Y. U. E., and Xinxin, W. A. N. G.: The Relationship of Ultra-Low Permeability Sandstone Aspect Ratio With Porosity, Permeability, Advances in Petroleum Exploration and Development, 7(1), 7-12, **2014**.

Hubert, J. F.: A zircon-tourmaline-rutile maturity index and the interdependence of the composition of heavy mineral assemblages with the gross composition and texture of sandstones, Journal of Sedimentary Research, 32(3), 440-450, **1962**.

Hurst, A., and Nadeau, P. H.: Clay microporosity in reservoir sandstones: an application of quantitative electron microscopy in petrophysical evaluation, AAPG bulletin, 79(4), 563-573, **1995**.

https://doi.org/10.5194/se-2020-47
Preprint. Discussion started: 4 May 2020

849 Iassonov, P., Gebrenegus, T., and Tuller, M.: Segmentation of X-ray computed tomography images of
850 porous materials: A crucial step for characterization and quantitative analysis of pore structures, Water
851 Resources Research, 45(9), **2009**.
852 Jackson, M. D., Muggeridge, A. H., Yoshida, S., and Johnson, H. D.: Upscaling permeability measurements
853 within complex heterolithic tidal sandstones, Mathematical Geology, 35(5), 499-520, **2003**.
854 Kalaydjian, F.: Origin and quantification of coupling between relative permeabilities for two-phase flows in
855 porous media, Transport in porous media, 5(3), 215-229, **1990**.
856 Kass, M., Witkin, A., and Terzopoulos, D.: Snakes: Active contour models, International Journal of
857 Computer Vision, 1(4), 321-331, **1988**.
858 Katz, A. J., and Thompson, A. H.: Quantitative prediction of permeability in porous rock, Physical Review
859 B, 34(11), 8179, **1986**.
860 Katz, A. J., and Thompson, A. H.: Prediction of rock electrical conductivity from mercury injection
861 measurements, Journal of Geophysical Research: Solid Earth, 92(B1), 599-607, **1987**.
862 Kerckhofs, G., Schrooten, J., Van Cleynenbreugel, T., Lomov, S. V., and Wevers, M.: Validation of x-ray
863 micro-focus computed tomography as an imaging tool for porous structures, Review of Scientific
864 Instruments, 79(1), 013711, **2008**.
865 Khan, F., Enzmann, F., and Kersten, M.: Multi-phase classification by a least-squares support vector
866 machine approach in tomography images of geological samples, Solid Earth, 7(2), 481-492, **2016**.
867 Kolodner, K., Avigad, D., Ireland, T. R., and Garfunkel, Z.: Origin of Lower Cretaceous ('Nubian')
868 sandstones of North-east Africa and Arabia from detrital zircon U-Pb SHRIMP dating, Sedimentology,
869 56(7), 2010-2023, **2009**.
870 Kozeny, J.: Uber kapillare leitung der wasser in boden, Royal Academy of Science, Vienna, Proceedings
871 Class I, 136, 271-306, **1927**.
872 Krinsley, D. H., Pye, K., Boggs Jr, S., and Tovey, N. K.: Backscattered scanning electron microscopy and
873 image analysis of sediments and sedimentary rocks. Cambridge University Press, **2005**.
874 Lenormand, R.: Sca2003-52: Interpretation of mercury injection curves to derive pore size distribution, in:
875 Proceedings of 2003 International Symposium of SCA., **2003**.
876 Li, Y., He, D., Chen, L., Mei, Q., Li, C., and Zhang, L.: Cretaceous sedimentary basins in Sichuan, SW
877 China: Restoration of tectonic and depositional environments, Cretaceous Research, 57, 50-65, **2016**.
878 Louis, L., David, C., Metz, V., Robion, P., Menendez, B., and Kissel, C.: Microstructural control on the
879 anisotropy of elastic and transport properties in undeformed sandstones. International journal of rock
880 mechanics and mining sciences, 42(7-8), 911-923, **2005**.
881 Massaad, M.: Origin and environment of deposition of Lebanon basal sandstones, Eclogae Geologicae
882 Helvetiae, 69(8), **1976**.
883 Mckay, G., Use of Adsorbents for the Removal of Pollutants from Wastewater. CRC press, **1995**.
884 Meyer, R., and Krause, F. F.: A comparison of plug-derived and probe-derived permeability in cross-bedded
885 sandstones of the Virgelle Member, Alberta, Canada: The influence of flow directions on probe
886 permeametry, AAPG bulletin, 85(3), 477-489, **2001**.

https://doi.org/10.5194/se-2020-47
Preprint. Discussion started: 4 May 2020

887 Mostaghimi, P., Blunt, M. J., and Bijeljic, B.: Computations of absolute permeability on micro-CT images,
888 Mathematical Geosciences, 45(1), 103-125, **2013**.
889 Narsilio, G. A., Buzzi, O., Fityus, S., Yun, T. S., and Smith, D. W.: Upscaling of Navier-Stokes equations in
890 porous media: Theoretical, numerical and experimental approach, Computers and Geotechnics, 36(7),
891 1200-1206, **2009**.
892 Nelson, P. H.: Pore-throat sizes in sandstones, tight sandstones, and shales, AAPG bulletin, 93(3), 329-340,
893 **2009**.
894 Neuzil, C. E.: Permeability of Clays and Shales, Annual Review of Earth and Planetary Sciences, 47, 247-
895 273, **2019**.
896 Niemi, A., Bensabat, J., Shtivelman, V., Edlmann, K., Gouze, P., Luquot, L., Shtivelman, V., Edlmann, K.,,
897 Liang, T., Fagerlund, ,F., Gendler, M., Goldberg, I., Tatomir, A., Lange, T., Sauter, M., and Freifeld, B.:
898 Heletz experimental site overview, characterization and data analysis for CO_2 injection and geological
899 storage, International Journal of Greenhouse Gas Control, 48, 3-23, **2016**.
900 Nordahl, K., and Ringrose, P. S.: Identifying the representative elementary volume for permeability in
901 heterolithic deposits using numerical rock models, Mathematical Geosciences, 40(7), 753, **2008**.
902 Nordahl. K., Ringrose, P. S., and Wen, R.: Petrophysical characterisation of a heterolithic tidal reservoir
903 interval using a process-based modelling tool, Petroleum Geoscience, 11, 17-28, **2005**.
904 Norris, R. J., and J. J. M. Lewis. The geological modeling of effective permeability in complex heterolithic
905 facies, in SPE Annual Technical Conference and Exhibition, Society of Petroleum Engineers, **1991**.
906 Okabe, H., and Oseto, K.: Pore-scale heterogeneity assessed by the lattice-Boltzmann method, Society of
907 Core Analysts (SCA2006-44), 12-16, **2006**.
908 Ovaysi, S., and Piri, M.: Direct pore-level modeling of incompressible fluid flow in porous media, Journal of
909 Computational Physics, 229(19), 7456-7476, **2010**.
910 Oyanyan, R. O., and Ideozu, R. U.: Sedimentological Control on Permeability Anisotropy and Heterogeneity
911 in Shorefae Reservoir, Niger Delta, Nigeria, International Journal of Science and Technology, 6(1),
912 **2016**.
913 Peksa, A. E., Wolf, K. H. A., and Zitha, P. L.: Bentheimer sandstone revisited for experimental purposes,
914 Marine and Petroleum Geology, 67, 701-719, **2015**.
915 Pettijohn, F. J., Potter, P. E., and Siever, R.: Sand and Sandstone. Springer Verlag, New York, **1972**.
916 Pyrcz, M. J., and Deutsch, C. V.: The whole story on the hole effect. Geostatistical Association of
917 Australasia, Newsletter, 18, 3-5, **2003**.
918 Renard, P., Genty, A., and Stauffer, F.: Laboratory determination of the full permeability tensor, Journal of
919 Geophysical Research: Solid Earth, 106(B11), 26443-26452, **2001**.
920 Reynolds, A. D.: Paralic reservoirs. Geological Society, London, Special Publications, 444(1), 7-34, **2017**.
921 Ringrose, P., and Bentley, M.: Reservoir Model Design: A Practitioner's Guide, Springer, 249 p. New York,
922 **2015**.
923 Rootare, H. M., and Prenzlow, C. F.: Surface areas from mercury porosimeter measurements, The Journal of
924 physical chemistry, 71(8), 2733-2736, **1967**.

https://doi.org/10.5194/se-2020-47
Preprint. Discussion started: 4 May 2020

925 Rustad, A. B., Theting, T. G., and Held, R. J.: Pore space estimation, upscaling and uncertainty modelling for
926 multiphase properties. In SPE Symposium on Improved Oil Recovery, Society of Petroleum Engineers,
927 **2008**.
928 Saltzman, U.: Survey of the southeastern flanks of Mount Hermon, Tahal report (in Hebrew), **1968**.
929 Sato, M., Panaghi, K., Takada, N., and Takeda, M.: Effect of Bedding Planes on the Permeability and
930 Diffusivity Anisotropies of Berea Sandstone, Transport in Porous Media, 127(3), 587-603, **2019**.
931 Schindelin, J., Arganda-Carreras, I., Frise, E., Kaynig, V., Longair, M., Pietzsch, T., Preibisch, S., Rueden,
932 C., Saalfeld, S., Schmid, B., Tinevez, J., White, D., Hartenstein, V., Eliceiri, K., Tomancak, P., and
933 Cardona, A.: Fiji: an open-source platform for biological-image analysis, Nature methods, 9(7), 676,
934 **2012**.
935 Schlüter, S., Sheppard, A., Brown, K., and Wildenschild, D.: Image processing of multiphase images
936 obtained via X-ray microtomography: a review, Water Resources Research, 50(4), 3615-3639, **2014**.
937 Schmitt, M., Halisch, M., Müller, C., and Fernandes, C. P.: Classification and quantification of pore shapes
938 in sandstone reservoir rocks with 3-D X-ray micro-computed tomography, Solid Earth, 7(1), 285-300,
939 **2016**.
940 Scholz, C., Wirner, F., Götz, J., Rüde, U., Schröder-Turk, G. E., Mecke, K., and Bechinger, C.: Permeability
941 of porous materials determined from the Euler characteristic, Physical review letters, 109(26), 264504,
942 **2012**.
943 Sethian, J. A.: A fast marching level set method for monotonically advancing fronts, Proceedings of the
944 National Academy of Sciences, 93(4), 1591-1595, **1996**.
945 Shaw, S. M.: Southern Palestine geological map on a Scale 1:250,000 with explanatory notes, Palestine
946 Geol. Soc. Publ., Jerusalem, **1947**.
947 Shenhav, H.: Lower Cretaceous sandstone reservoirs, Israel: petrography, porosity, permeability, AAPG
948 Bulletin, 55(12), 2194-2224, **1971**.
949 Sheppard, A. P., Sok, R. M., and Averdunk, H.: Techniques for image enhancement and segmentation of
950 tomographic images of porous materials, Physica A: Statistical mechanics and its applications, 339(1-2),
951 145-151, **2004**.
952 Shimron, A. E. and Peltz, S.: Early Cretaceous pyroclastic volcanism on Mount Hermon Range, Geological
953 Survey of Israel, Report GSI/10/98, **1993**.
954 Shimron, A. E.: Tectonic evolution of the southern Mount Hermon, Geological Survey of Israel Report,
955 GSI/10/98, **1998**.
956 Sneh, A., and Weinberger, R.: Geology of the Metula quadrangle, northern Israel: Implications for the offset
957 along the Dead Sea Rift, Israel Journal of Earth Sciences, 52, **2003**.
958 Sneh, A., and Weinberger, R.: Metula sheet 2-11, Geology Survey of Israel, Ministry of Energy, **2014**.
959 Tatomir, A. B., Halisch, M., Duschl, F., Peche, A., Wiegand, B., Schaffer, M., Licha, T., Niemi, A.,
960 Bensabat, J., and Sauter, M.: An integrated core-based analysis for the characterization of flow, transport
961 and mineralogical parameters of the Heletz pilot CO_2 storage site reservoir, International Journal of
962 Greenhouse Gas Control, 48, 24-43, **2016**.

https://doi.org/10.5194/se-2020-47
Preprint. Discussion started: 4 May 2020

963 Tiab, D., and Donaldson, E. C.: Petrophysics: Theory and Practice of Measuring Reservoir Rock and Fluid
964 Transport Properties, Elsevier, **2004**.
965 Tidwell, V. C., and Wilson, J. L.: Permeability upscaling measured on a block of Berea Sandstone: Results
966 and interpretation, Mathematical Geology, 31(7), 749-769, **1999**.
967 Vincent, L., and Soille, P.: Watersheds in digital spaces: an efficient algorithm based on immersion
968 simulations, IEEE Transactions on Pattern Analysis & Machine Intelligence, 6, 583-598, **1991**.
969 Vogel, H. J.: Topological characterization of porous media, in: Morphology of condensed matter, edited by:
970 Mecke, K. R., and Stoyan, D., Springer, Berlin, 75-92, **2002**.
971 Weissbrod, T.: Stratigraphy and correlation of the Lower Cretaceous exposures across the Dead Sea
972 Transform with emphasis on tracing the Amir Formation in Jordan, Israel Journal of Earth Sciences,
973 51(2), 55–78, **2002**.
974 Weissbrod, T., and Nachmias, J.: Stratigraphic significance of heavy minerals in the late Precambrian-
975 Mesozoic clastic sequence ("Nubian Sandstone") in the Near East, Sedimentary Geology, 47(3-4), 263-
976 291, **1986**.
977 Whitaker, S.: Flow in porous media I: A theoretical derivation of Darcy's law, Transport in porous media,
978 1(1), 3-25, **1986**.
979 Wildenschild, D., and Sheppard, A. P.: X-ray imaging and analysis techniques for quantifying pore-scale
980 structure and processes in subsurface porous medium systems, Advances in Water Resources, 51, 217-
981 246, **2013**.
982 Wilson, M., Shimron, A. E., Rosenbaum, J. M., and Preston, J.: Early Cretaceous magmatism of Mount
983 Hermon, Northern Israel, Contributions to Mineralogy and Petrology, 139(1), 54-67, **2000**.
984 Worden, R. H., and Burley, S. D.: Sandstone diagenesis: the evolution of sand to stone, Sandstone
985 Diagenesis: Recent and Ancient, 4, 3-44, **2003**.
986 Zhang, D., Zhang, R., Chen, S., and Soll, W. E.: Pore scale study of flow in porous media: Scale
987 dependency, REV, and statistical REV, Geophysical research letters, 27(8), 1195-1198, **2000**.

988

https://doi.org/10.5194/se-2020-47
Preprint. Discussion started: 4 May 2020


Solid Earth Discussions

Appendix A: Description of the Hatira Formation

The Hatira Fm. is the lower part of the Kurnub Group of Lower Cretaceous (Neocomian – Barremian) age. The Hatira Fm. nomenclature used in Israel and Jordan is equivalent to Grès de Base in Lebanon (Massaad, 1976). This formation occurs in Israel in outcrops from the Eilat area along the rift valley, in the central Negev, and in the northernmost outcrops on Mount Hermon; it forms part of a large Palaeozoic – Mesozoic platform and continental margin deposits in northeastern Africa and Arabia. The Hatira Fm. consists of siliciclastic units, typically dominated by quartz-rich sandstones (Kolodner et al., 2009 and references therein). The underlying Palaeozoic sandstones cover large areas in North Africa and Arabia from Morocco to Oman; these sandstones overlie a Precambrian basement affected by Neoproterozoic (pan African) orogenesis (Garfunkel, 1988, 1999; Avigad et al., 2003, 2005). The lower Palaeozoic sandstones in Israel and Jordan originated from the erosion of that Neoproterozoic basement, the Arabian-Nubian Shield, with contributions from older sources. These lower Palaeozoic sandstones (Cambrian and Ordovician) are described as first-cycle sediments (Weissbrod and Nachmias, 1986; Amireh, 1997; Avigad et al., 2005). Exposures of the Hatira Fm. in the Central Negev, the Arava Valley, Eilat and Sinai were originally defined as the Wadi (Kurnub) Hatira Sandstone (Shaw, 1947). The largely siliciclastic section of the Hatira Fm. is intercalated with carbonates and shales representing marine ingressions that increase towards the north (Weissbrod, 2002).

The Lower Cretaceous sandstones of the Kurnub Group are described as super mature, cross-bedded, medium- to fine-grained, moderately sorted to well-sorted quartz arenites with a high zircon-tourmaline-rutil (ZTR) index (for more details, see Kolodner (2009)). Earlier observations indicate the relatively scarce occurrence of siltstones and claystones compared to sandstones (Massaad, 1976; Abed, 1982; Amireh, 1997). These Lower Cretaceous sandstones are mainly the recycled products of older siliciclastic rocks throughout the Phanerozoic; the sand was first eroded from the surface of the pan African orogeny ca. 400 Ma prior to its deposition in the Lower Cretaceous sediments (Kolodner et al., 2009).

The Mount Hermon block was located at the southern border of the Tethys Ocean during the Early Cretaceous (Bachman and Hirsch, 2006). A paleo-geographical reconstruction indicates that the sandy Hatira Fm. (Fig. 1) was deposited in a large basin, which included both terrestrial and coastal environments such as swamps and lagoons (Sneh and Weinberger, 2003). The Hermon block, located next to the Dead Sea

https://doi.org/10.5194/se-2020-47
Preprint. Discussion started: 4 May 2020

Solid Earth
Discussions
Open Access
EGU

Transform, was rapidly uplifted during the Neogene (Shimron, 1998). The area is marked by intense erosion, which resulted in extensive outcrops such as those near Ein Kinya on the southeastern side of Wadi E'Shatr.

Appendix B: Results of the REV determination by the classical approach

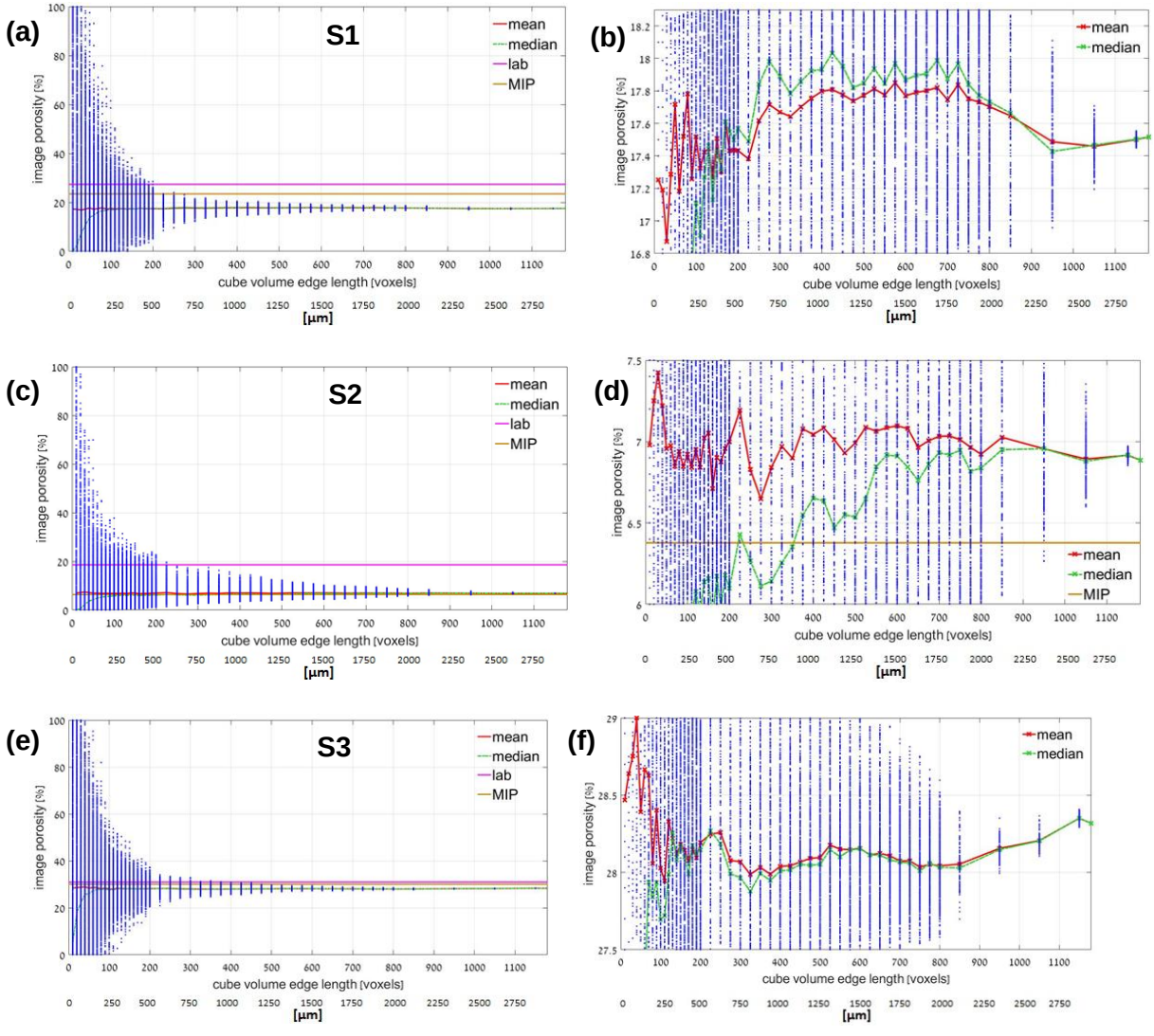

https://doi.org/10.5194/se-2020-47
Preprint. Discussion started: 4 May 2020

Figure B1. *Results of the classic REV analysis for sandstones S1-S3* ***(a,c,e)****.* ***(b, d, f)*** *Magnified views of the mean and median porosity trends of S1-S3 calculated for varying edge lengths. The scattering of porosity measured for each sub-volume is shown in blue dots. The laboratory porosities measured by gas porosimetry are shown by a pink line. The image porosity for CT, which was predicted by MIP for the resolution limit, is shown by a yellow line. The mean and median porosity are depicted by red and green lines, respectively.*

Appendix C: Euler characteristic

The Euler characteristic is a number that describes the structure of a topological space. The most intuitive way to think about the Euler characteristic is in terms of its Betti numbers (β_i):

$$\chi = \beta_0 - \beta_1 + \beta_2$$

For a 3D object, β_0 is the number of components, β_1 is the number of inequivalent loops and β_2 is the number of cavities (enclosed voids). In describing the topology of the pore space of a porous rock, it can be assumed that the solid matrix is connected such that $\beta_2 = 0$. In this case, the Euler number reduces to the difference between the number of discrete components and the number of inequivalent loops. If all pore spaces are connected via one pathway or another and assuming that there are no isolated pore spaces, then $\beta_0 = 1$. In a pore network of sandstone that can be modeled as a bundle of tubes, the number of loops β_1 is large, and χ is negative. Therefore, the Euler number, χ, is related to the connectivity of the pore space. As the number of loops decreases, the Euler number becomes less negative and eventually becomes positive, where the system will no longer percolate, according to Vogel (2002).

https://doi.org/10.5194/se-2020-47
Preprint. Discussion started: 4 May 2020

Solid Earth
Discussions
Open Access
EGU

Appendix D: Maximal hydraulic conductance

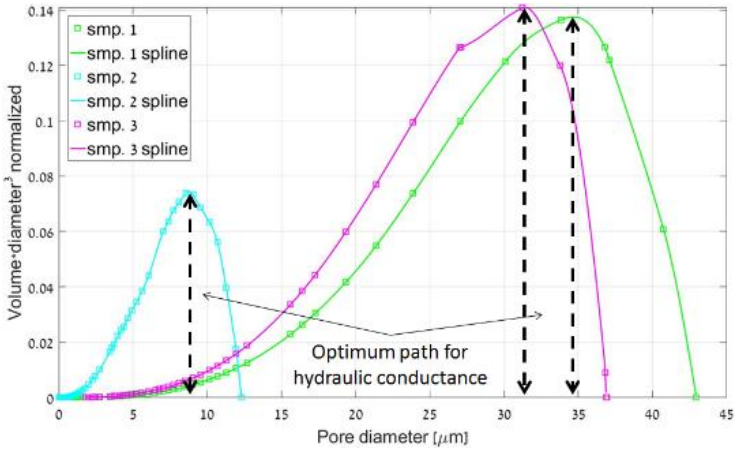

Figure D1. *The pore throat length of the maximal hydraulic conductance, l_{max}, is defined from the maximal (normalized) hydraulic conductance (Katz and Thompson, 1987), specified at the vertical axis of the chart. The corresponding pore throat diameters (x-axis) marked by black arrows define the pore throat diameters (or pore throat lengths of maximal conductance), l_{max}, where all connected paths composed of $l \geq l_{max}$ contribute significantly to the hydraulic conductance (see Sect.3.2).*